Zn-doped mesoporous hydroxyapatites and their antimicrobial properties

Cleibson Oliveira de Lima, André Marcorin de Oliveira, Edson Silva Filho, Laís Chantelle, Maguy Jaber, Maria Gardênia Fonseca

Zn-doped mesoporous hydroxyapatites and their antimicrobial properties

Cleibson Oliveira de Lima,[a] André L. Menezes de Oliveira,[a] Laís Chantelle,[a] Edson C. Silva Filho,[b] Maguy Jaber,[c] Maria Gardênia Fonseca[a,*]

[a]*Universidade Federal da Paraíba, Núcleo de Pesquisa e Extensão LACOM, 58051-085, João Pessoa, Paraíba, Brazil.*

[b]*Interdisciplinary Laboratory for Advanced Materials-LIMAV, Universidade Federal do Piauí, Teresina, 64049- 11 550, Piauí, Brazil.*

[c]*Sorbonne Université, Laboratoire d'Archéologie Moléculaire et Structurale, Institut Universitaire de France (IUF), CNRS UMR 8220, UPMC – Tour 23, 3ème étage, couloir 23-33, BP 225, 4 place Jussieu, 75005 Paris, France.*

*mgardennia@quimica.ufpb.br

Phone/Fax +55833216-7433

Statistical summary of the article

Word count - Title page, text, figures captions, and tables, but not references – 5457 words
Word count – Title page, text, figures captions, tables, and references – 7654 words
Number of Figures – 6
Number of Table - 2

Graphical abstract

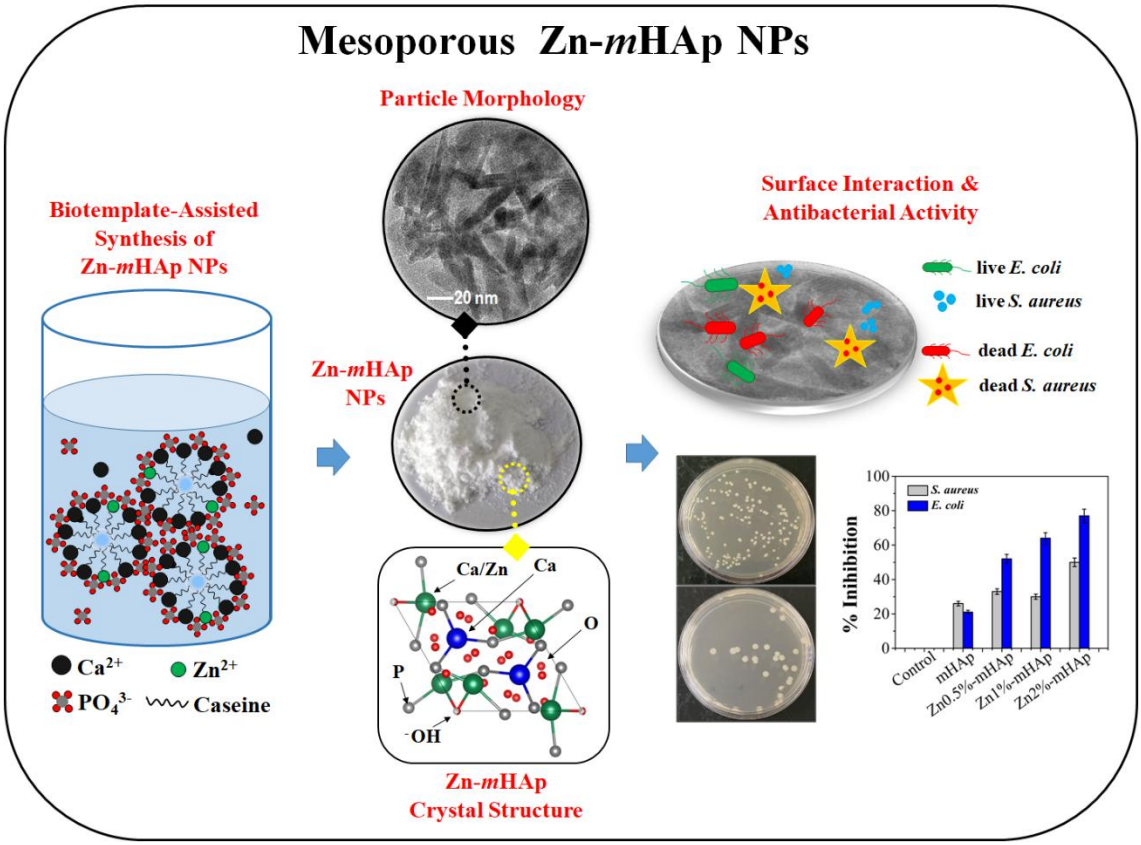

Highlights

- Pure and Zn-doped mesoporous hydroxyapatites were synthesized via casein biotemplating
- Formation of mesoporous biomaterials is strongly dependent on biotemplating and Zn doping
- Zn-rich mesoporous hydroxyapatites showed a high surface area of 182 m^2 g^{-1}
- Antimicrobial activity of the hydroxyapatites depended on their Zn^{2+} content and mesoporous surface
- Zn-hydroxyapatite showed the strongest inhibitory effect against Gram-positive bacteria stain.

Abstract

Recently, zinc-based materials have gained immense attention as antimicrobial agents. In this study, zinc-doped mesoporous hydroxyapatites (HAps) with various Zn contents were prepared by co-precipitation using a phosphoprotein as the porous template. The use of the phosphoprotein as the porous template resulted in the formation of zinc-doped mesoporous HAps (mHAps) with large pores and specific surface area (182 $m^2 g^{-1}$), as indicated by the nitrogen adsorption/desorption measurements. The formation of the zinc-doped HAps was confirmed by various analytical techniques such as X-ray diffraction, Fourier transform infrared spectroscopy, transmission electron microscopy, and X-ray photoelectron spectroscopy. The biomaterials prepared in this study were used as antimicrobial agents against gram-positive (*Staphylococcus aureus*) and gram-negative (*Escherichia coli*) bacteria. The Zn2%-mHAp sample showed the maximum bacterial inhibitory concentrations of 50±5% and 77±5% for the gram-positive and gram-negative bacteria, respectively. The antibacterial activity of the mHAp samples depended strongly on their Zn^{2+} content. Thus, the use of a biotemplate and Zn^{2+} ions is an efficient approach for the formation of novel HAp-based biomaterials with promising antibacterial properties. This synthesis approach will pave a new pathway for the functionalization of other materials for different biomedical applications.

Keywords: Hydroxyapatite; biomaterial; zinc; template; antibacterial.

1. Introduction

The emergence of bacterial strains resistant to the multiple antibiotics used worldwide is a huge health challenge, as bacteria are a major cause of chronic infections and mortality. Therefore, the development of novel efficient antimicrobial agents is imperative [1]. Both inorganic and organic materials and their combinations have been used as antimicrobial agents against gram-positive and gram-negative bacteria. Among the various antimicrobial inorganic materials investigated till date, oxides such as titanium oxide [2,3], silver oxide [4], and zinc oxide [5–7] and phosphates such as pure hydroxyapatite (HAp) [8], HAp doped with different cations including zinc [9], silver [10–12], cerium [13,14], strontium [15], copper [16], and titanium [17] have been extensively investigated.

HAp ($Ca_{10}(PO_4)_6(OH)_2$) is an inorganic biomaterial with great potential for biomedical applications such as in dentistry because of its biocompatibility, bioactivity, and osteoconductivity [18]. The biological and physicochemical properties of synthetic HAp can be improved through various chemical modification processes such as cationic and anionic doping [19,20]. The dopants incorporated into the HAp network can affect its crystallinity, particle morphology, surface charges, dissolution/reabsorption rates, densification, mechanical resistance, and thermal stability [21]. Zn^{2+} is one of the most promising dopants used to modify the properties of HAp. This is because Zn^{2+} is present in bones; acts as a cofactor for enzymes; and contributes to the metabolism of proteins, carbohydrates, and lipids [19,22–24].

Hence, various studies have been carried out to prepare Zn-doped HAps for application as antimicrobial agents [24–26] such as in bone grafting, coatings on metallic implants because of their high biocompatibility and bioactivity, in bone

mineralization [27–29], and for improving the adhesion between osteoblasts. The properties of HAp for orthopedic and dental applications have also been investigated [30,31]. For example, Mg^{2+}-, Zn^{2+}-, Sr^{2+}-, and Si^{4+}-doped HAp/chitosan composites are obtained by co-precipitation and are used for biomedical applications [21]. It has been reported that Zn^{2+}-doped HAp/chitosan promotes *in-vitro* cell proliferation and is a promising material for bone implants. The Zn^{2+}-doped apatite coating on titanium rods used as bone implants induces fibroblastic proliferation, *in-vitro* osteoblastic proliferation, and differentiation around the implant and reduces the infections in bone fixation pin linings [29].

In a previous study, Tank et al. [32] synthetized nano Zn^{2+}-doped HAps with approximately 1, 3, and 5 mol% Zn^{2+} by co-precipitation mediated by a nonionic surfactant (Triton X-100) and were tested against *Staphylococcus aureus* (*S. aureus*), *Micrococcus luteus*, *Bacillus cereus*, *Shigella flexneri*, and *Pseudomonas aeruginosa* [32]. The authors evidenced that Zn^{2+}-doped HAps showed good antimicrobial activity against gram-positive bacteria, but no meaningful efficiency was observed against gram-negative bacteria. In the research conducted by Ofudje et al. [9], Zn^{2+}-doped HAps with 5, 10, 15, and 20 mol% Zn^{2+} were prepared via co-precipitation also exhibit excellent antibacterial activity against *Escherichia coli (E. coli).* The antibacterial activity of HAps increased with an increase in the Zn^{2+}concentration [9]. More recently, Ullah et al. [33] reported the synthesis of Zn^{2+}- and Sr^{2+}-codoped HAps using a hydrothermal method. These HAps showed efficient antibacterial activity against *S. aureus* and *E. coli*. They also show increased proliferation, fixation, and cell adhesion compared to pure HAp [33].

There is no consensus on the type of antibacterial action mechanism prevalent in nanoparticulate materials, including HAp-based biomaterials. However, three principal

mechanisms have been reported for antimicrobial action in the presence of Zn^{2+}-containing nanoparticles. According to the first mechanism, the Zn^{2+} ions bind to the proteins in the bacteria and deactivate them. The second mechanism proposes that the interaction of Zn^{2+} ions with the bacterial membrane leads to structural changes in the biomaterial and an increase in its permeability, resulting in the death of the microorganisms. According to the third mechanism, the interaction between the Zn^{2+} ions and microbial nucleic acids interrupts the replication of microorganisms [34,35]. However, the other antimicrobial actions include damage to the plasma membrane and cell wall, inhibition of electron transport, blocking cell division, and production of reactive oxygen species (ROS) with the functional groups of proteins and nucleic acids such as mercapto (–SH), amino (–NH), and carboxyl (–COOH), which can impair enzymatic activity, alter the cell structure, and affect the normal physiological processes, and thus inhibit the growth of the microorganisms, causing even cell death [36,37]. In addition, electrostatic, van der Waals, hydrophobic, and ligand-receptor interactions can occur between the bacterial cells and nanoparticles. Ligand-receptor interactions have been proposed as the dominant antimicrobial action mechanism in the presence of weak repulsive electrostatic interactions [25].

The synthesis of HAps doped with different ions has been extensively investigated. In addition, the use of a template can lead to the formation of mesoporous HAps with different surface areas, particle sizes, and pore volumes, and hence can expand the range of their applications [38–40]. Despite the number of reported studies concerning HAp materials, the synthesis of Zn^{2+}-doped mesoporous HAp using a biotemplate and their use as antimicrobial agents has not yet been reported. In relation to applications in biomedical field, mesoporous materials are important for drugs delivery systems [41].

In addition, mesoporous materials can used as carrier of larger biological molecules [38] and scaffolds for bone tissue regeneration [41].

Motivated by the above-mentioned works and in order to develop novel HAp-based biomaterials with specific characteristics and properties, in this study, we synthesized for the first time, Zn^{2+}-doped mesoporous HAp biomaterials via co-precipitation using a phosphoprotein (casein) as the template. The effect of the low amount of Zn^{2+} content (0.5, 1, and 2 mol%) on the structural and textural features of the biomaterials was investigated. The antibacterial activity of the biomaterials for gram-positive (*S. aureus*) and gram-negative (*E. coli*) bacteria were investigated. Unlike previous studies concerning Zn-doped HAp, biomaterials with mesoporous characteristics with large surface area were obtained in the present work. It is also important mentioning that the use of casein as a biotemplate for the synthesis of Zn^{2+}-doped mesoporous HAps may still enhance the bioactivity and biocompatibility of the synthetic mHAp systems obtained in the present work. The findings of this study will pave a new pathway for the synthesis of novel HAp-based materials and other mesoporous biomaterials for different biological applications.

2. Experimental

2.1. Chemicals

Ammonium phosphate ($(NH_4)_2HPO_4$, *Merck*, 99%), calcium chloride ($CaCl_2 \cdot 2H_2O$ *Sigma-Aldrich*, 93%), zinc nitrate ($Zn(NO_3) \cdot 6H_2O$, *Vetec*, 97%), casein from bovine milk (*Reagen*, 99%), and sodium hydroxide (NaOH, *Vetec*, 97%) were used as received without further purification. Used casein is a mixture of phosphoproteins that contains all of the common amino acids, and any purification or

isolation of specific type was performed prior to use. Deionized water was used in all the procedures.

2.2. Synthesis of pure and doped mesoporous HAps

Mesoporous HAp (mHAp) was prepared according to a previously reported method [38]. Initially, a 0.2 mol L^{-1} NaOH solution was prepared and 1.25 g of casein was added to 250 mL of this solution. The resulting solution was mechanically stirred at 1200 rpm for 1 h at 30 °C to form a white suspension. Then, the agitation speed was decreased to 200 rpm and 250 mL of $(NH_4)_2HPO_4$ and $CaCl_2 \cdot 2H_2O$ were simultaneously added to the system at 2 mL min^{-1}. The amounts of calcium and phosphate used in the synthesis procedure were 0.056 and 0.033 mol, respectively. The resulting white precipitate was aged for 24 h at 30 °C, and the solid part was recovered by filtration and was then washed with distilled water until a negative chloride test was achieved. Finally, the solid was dried at 100 °C in a furnace for 24 h followed by calcination at 500 °C for 12 h in an O_2 atmosphere at a heating rate of 2 °C min^{-1} in order to eliminate the casein template. The obtained sample was labeled as mHAp.

The same procedure was used for the synthesis of the zinc-doped HAps by adding a zinc nitrate solution to the system simultaneously with the addition of the calcium and phosphate salts. The Zn^{2+} doping amount was varied (0.25, 0.5, and 1.0 mmol L^{-1}). The zinc-doped samples were labeled as Zn*x*-mHAp (where x = 0.5, 1, and 2 mol%).

2.4. Characterization

The powder X-ray diffraction (XRD) patterns of the samples were recorded on a Shimadzu diffractometer 6000 model equipped with CuKα monochromatic radiation (λ

= 0.154 nm) and operating at 30 kV and 30 mA. The XRD patterns were recorded over the 2θ range of 5–50° with a step size of 0.02° at a scan rate of 0.05 °min^{-1}.

The lattice parameters of the samples were determined using the (0 0 2), (1 0 2), (2 1 0), (2 1 1), (3 1 0), and (2 2 2) Bragg diffraction reflections of the hexagonal crystal structure of HAp (ICDD 00-009-0432). The crystallite size of the samples was calculated using the Scherrer equation as follows:

$$D = \frac{0.9 \times \lambda}{\beta \times cos\ \theta} (1)$$

where D is the average crystallite size, λ is the wavelength, θ is the diffraction angle, and β is the line broadening at half the maximum intensity (full width at half maximum, FWHM) of the peak after subtracting the instrumental line broadening.

The Fourier transform infrared (FTIR) spectra of the samples were recorded on an IR Prestige–21Shimadzu spectrophotometer in the transmittance mode using the KBr pellet method. For each spectrum, a set of 30 consecutive scans were collected over the wavenumber range of 4000–400 cm^{-1} at a resolution of 4 cm^{-1}.

The transmission electron microscopy (TEM) images of the samples were obtained using a FEI-Tecnai G2 Spirit Biotwin microscope operating at 120 kV. The samples were suspended in isopropyl alcohol and were then deposited on 400 mesh copper grids covered with an ultrafine carbon layer with a thickness of 2–3 nm. The high-resolution TEM (HR-TEM) analysis of the samples was carried out using a JEOL 100CX microscope operating at 200 kV. The TEM images were processed using ImageJ software (version 1.53a). To generate the particle size distribution histograms of the samples, approximately 250 particles were counted. For the HRTEM analysis, the fast Fourier transform (FFT) and inverse fast Fourier transform (IFFT) of the samples were

calculated in order to isolate the dots from the noise to recompense the microscopy images. Thus, a clear image was obtained, providing the crystallographic planes from which the corresponding *d* spacing was calculated.

The nitrogen adsorption/desorption measurements of the samples were carried out on an ASAP 2420 Micrometrics system. The specific surface areas of the samples were calculated using the Brunauer-Emmett-Teller method [42]. The pore diameters and volume distributions of the samples were measured using the Barret-Joyner-Halanda method [43]. The thermogravimetry (TG) curves of the samples were recorded on a Netzsch STA 449F3 instrument. For the TG analysis, 10 mg of the samples were transferred into alumina crucibles, which were then heated to 1000 °C in a nitrogen atmosphere at a flow rate of 50 mL min^{-1} and a heating rate of 10 °C min^{-1}.

The X-ray photoelectron spectroscopy (XPS) profiles of the samples were obtained using a VSW HA-100 spherical analyzer with an AlKα radiation (hν = 1486.6 eV). The high-resolution spectra of the samples were obtained at a constant analyzer pass energy of 44 eV. The surface charging was corrected for all the spectra, shifting them in relation to the C1s line at 284.6 eV, and the curve fitting was performed using a Gaussian line shape by subtracting the Shirley background.

2.3. *In-vitro* antimicrobial activity

The direct contact method was used to investigate the antibacterial activity of the biomaterials according to a previously reported procedure [44]. Mueller Hinton agar was used as the growth medium. The growth medium was hydrated using 36 g of medium per 1000 mL of distilled water. After the hydration process, the Mueller Hinton agar solution (pH 7.3 ± 0.1) was heated until the agar dissolved completely. The

solution was then transferred to an autoclave and heated to 121 °C for 15 min. After plating, the culture medium was subjected to the sterility test in a microbiological oven for 24 h.

The test was carried out on a mixture of 2000 μL of inoculum in 10^{-4} $CFUmL^{-1}$ of *S. aureus* (ATTC 25923) and *E. coli* (ATTC 25922) and approximately 2000 μg of the biomaterials (mHAp and Zn*x*-mHAp). An aliquot of 200 μL was withdrawn and spread vertically, horizontally, and diagonally over the growth medium with a Drigalski loop on the Petri dish. The plate was kept in a microbiological oven for 24 h. Then, the colony-forming units (CFUs) were counted. The tests were performed in triplicate for each of the biomaterials. Positive bacterial growth control (0.85% saline) was prepared to compare and verify the viability of the strains.

3. Results and discussion

3.1. Textural properties

The textural properties of the samples were investigated by carrying out their N_2 adsorption/desorption measurements (**Figure SM1**, **Table 1)**. All the samples prepared using casein showed type-IV isotherms with type-H1 hysteresis at P/P_o= 0.75 and 1.0, which are characteristic of typical mesoporous materials having regular pores with cylindrical or polyhedral shapes and open edges [45].

Table 1. Textural properties for pure and zinc-doped mesoporous HAps.

Sample	SSA_{BET} ($m^2\ g^{-1}$)	V_p* ($cm^3\ g^{-1}$)	D_p^* (nm)
mHAp	138 ± 3.0	0.55	14.7
Zn0.5%-mHAp	180 ± 2	0.49	10.9

Zn1%-mHAp	170 ± 3.0	0.49	11.5
Zn2%-mHAp	182 ± 4.0	0.50	11.1

*V_p and D_p are volume and diameter of pore, respectively.

The HAps prepared in this study showed a specific surface area (SSA) of 138–182 m^2 g^{-1}, which is higher than those reported previously for HAps. In a previous study, Pure mHAp and HAp coated with iron oxide (HAp-Fe_2O_3) were synthesized using the F-127 triblock copolymer as the template and sucrose [46]. The resulting pure HAp and HAp-Fe_2O_3 samples showed the SSA values of 141 and 148 m^2 g^{-1}, respectively [46]. On the other hand, mHAp synthesized using vitamin C as template shows an SSA of 62–88 m^2 g^{-1} [47]. HAp synthesized using CTAB as template shows a low specific surface area of 62 m^2 g^{-1} [48]. In addition, mHAp prepared via the co-precipitation method using casein as template shows an SSA of 54–106 m^2 g^{-1} [38]. Zn-doped HAp prepared via co-precipitation with no template shows an SSA of 99–115 m^2 g^{-1}[23].

As the pore size distribution of a material is closely related to its total area, it is an important parameter for investigating the structural properties of porous materials. As can be observed from the inset of **Figure SM1** and **Table 1**, the average pore diameter of the HAps prepared in this study varied from 10.9 to 14.7 nm. This indicates that the addition of Zn^{2+} to the HAp structure as well as the use of the template favored the formation of small and uniformly distributed pores (**Figure SM1**) as compared to the previously reported mHAps with the pore sizes of 3.17–5.8 [49] and 5.4–12.2 nm and an SSA of 46.5 m^2 g^{-1} [50].

3.2 XRD patterns

The XRD patterns of the pure and zinc-doped HAps are shown in **Figure 1.** The diffraction patterns of the synthesized samples showed broad diffraction peaks, which are characteristic of nanostructured materials. The diffraction peaks of the samples could be indexed to the hexagonal phase of HAp with the *P63/m* space group. In addition, no secondary phases were detected in the XRD patterns of the Zn-doped HAps, indicating the formation of stable Zn*x*-HAp compounds irrespective of the Zn^{2+} content. This is consistent with the results obtained in a previous study [32].

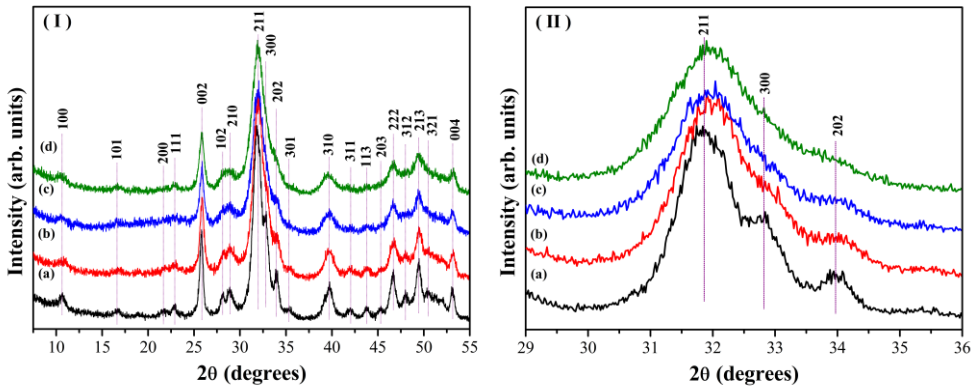

Figure 1. (I) XRD patterns and (II) magnified XRD patterns over the 2θ range of 30–36° for (a) mHAp, (b) Zn0.5%-mHAp, (c) Zn1%-mHAp, and (d) Zn2%-mHAp.

The presence of Zn^{2+}cations in the mHAp structure resulted in an increase in the long-range structural disorder, as evidenced by the broadening of the (211) reflection peak, which merged with the reflections corresponding to the (112) and (300) planes. The calculated FWHM values indicated that an increase in the amount of Zn^{2+} resulted in an increase in the long-range structural disorder of the samples (**Figure SM2).** This resulted in a lower decrease in the crystallite size (calculated using the Scherrer equation) of all the Zn*x*-mHAp samples. This behavior can be attributed to the increase

in the number of nucleation sites due to the presence of Zn^{2+} cations in the solution. The increase in the number of nucleation sites inhibited the growth of crystallites, which also decreased the crystallinity of the material. These results are consistent with those reported previously [51–54]. In addition, the casein micelles acted as a template to control the pore distribution and particle growth. This significantly affected the crystallite growth of the pure and Zn-doped HAp samples. A similar phenomenon has been reported previously for pure HAp.

In order to further investigate the structural properties of the Zn*x*-mHAp samples and the effect of the Zn^{2+} doping amount on the structure of HAp, the lattice parameters of the samples were calculated and are listed in **Table 2**. As expected, the addition of Zn^{2+} to mHAp caused changes in its lattice parameters, *a* and *c*, as well as the unit cell volume, *V*. As the ionic radius (r) of Ca^{2+} ($r_{Ca}{}^{2+}$ = 1.00 in coordination number (CN) 6) is larger than that of Zn^{2+} ($r_{Zn}{}^{2+}$ = 0.74, CN = 6) [55], the substitution of Ca^{2+} by Zn^{2+} is favorable for the formation of the HAp structure and results in an increase in the lattice parameters, as observed in this study [51,52,54]. For instance, X-ray absorption fine structure measurements have revealed that Zn^{2+} cations preferentially occupy the Ca^{2+} sites in Zn-doped HAp [51]. Compared to standard HAp, the Zn*x*-mHAp samples showed increased lattice parameters and unit cell volume because of the use of casein as the template in the synthesis process.

Table 2. Lattice parameters of the synthesized pure and Zn-doped mHAp solids.

Solid	Lattice parameters (Hexagonal)		Unit cell volume
	a (nm)	**c (nm)**	**V (nm^3)**
Standard HAp*	0.941	0.688	52.80
mHAp	0.944 ± 0.008	0.688 ± 0.013	53.12

Zn0.5%-mHAp	0.942 ± 0.014	0.684 ± 0.024	52.59
Zn1%-mHAp	0.944 ± 0.012	0.686 ± 0.022	52.91
Zn2%-mHAp	0.947 ± 0.020	0.683 ± 0.034	53.09

*ICDD 00-009-0432

3.2. FTIR spectroscopy

The FTIR spectra of the mHAp and Zn*x*-mHAp samples are shown in **Figure 2,** and the assignments of the IR bands are summarized in **Table SM1.**

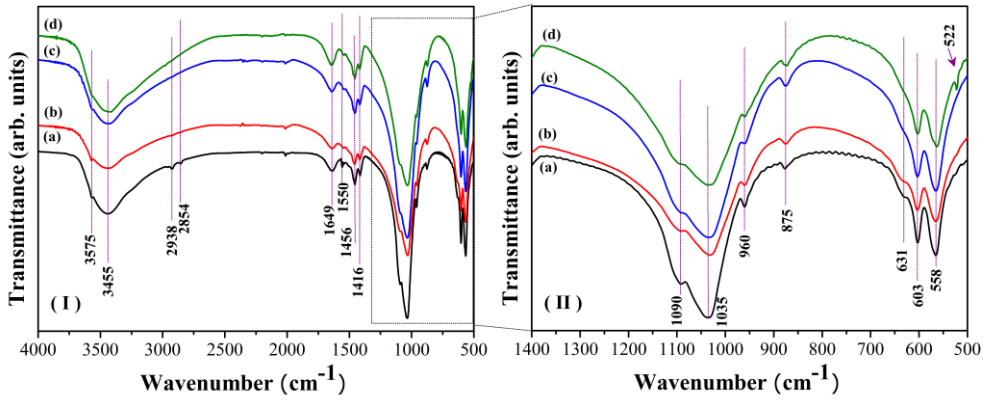

Figure 2. Infrared spectra in the (I) 4000–400 cm^{-1} and (II) 500–1400 cm^{-1} regions for the (a) mHAp, (b) Zn0.5%-mHAp, (c) Zn1%-mHAp, and (d) Zn2%-mHap samples.

The FTIR spectra of the samples showed bands characteristic of HAp in the region below 1100 cm^{-1}. This is consistent with the results reported previously [38,56,57]. The bands at 1090, 1035, and 960 cm^{-1} can be attributed to the asymmetric deformation of PO_4^{3-} and the stretching of P-OH in HPO_4^{2-}, while the band at 875 cm^{-1} corresponds to the P-O(H) deformation [38,48,58]. Bands at 603 and 558 cm^{-1} are assigned to PO_4^{3-} vibrations and P-O(H) asymmetric deformation in HPO_4^{2-},

respectively [59]. The additional bands at 3575 and 3455 cm^{-1} can be attributed to the OH stretching of the structural groups in HAp and the OH groups of the adsorbed water [60]. The OH deformation band of the water molecules was also observed at 1649 cm^{-1} [61]. Considering that the samples were synthesized in the presence of casein, the appearance of low-intensity bands at 2938 and 2854 cm^{-1} in the case of the mHAp sample can be attributed to the C-H asymmetric and symmetric stretching of casein [38], respectively. The band at 1550 cm^{-1} corresponds to amide II resulting from the combination of the C–N stretching and N–H deformation [62]. The other bands observed at 1456 and 1416 cm^{-1} correspond to the CH_2 and C-OH deformations, respectively. These results confirm the presence of casein in the samples [38].

In addition to the characteristic bands of HAp and casein, an additional band was observed at 522 cm^{-1} in the spectrum of Zn2%-mHAp, attributed to the P-O···Zn and P···O-Zn bonds (P-O-Zn) [59][63]. This band was not observed in the spectra of the samples with less than 2% (mol concentration) Zn^{2+}. This is consistent with the results reported previously for Zn-doped mHAps of the type $Ca_{10-x}Zn_x(PO_4)_6(OH)_2$ ($0 \leq x \leq$ 70%) [52].

3.4. TG analysis

The TG curves of the samples are shown in **Figure SM3,** and the results are summarized in **Table SM2**.

All the HAp samples showed three mass loss events over different temperature ranges (**Table SM2)**. The mHAp, Zn0.5%-mHAp , Zn1%-mHAp, and Zn2%-mHAp samples showed the first mass losses of 2.7%, 2.5%, 4.1%, and 3.4%, respectively, attributing to the loss of the adsorbed water [64]. These samples showed the second mass losses of 1.8%, 1.8%, 1.9%, and 2.1%, respectively, attributing to the OH^-

condensation and loss of the organic material associated with the remaining casein [38,56]. The presence of casein was also detected by FTIR spectroscopy, as discussed in the previous section. The samples showed the third mass losses of 1.0%, 1.5%, 1.9%, and 1.8%, respectively, attributing to the decomposition of HAp [65].

3.5. TEM and HR-TEM analyses

The TEM images of the samples are shown in **Figure SM4**. The morphologies, particle sizes, and porous structures of the samples were investigated from these images. **Figure 3** shows the HR-TEM images of Zn1%-mHAp.

All the TEM images (**Figure SM4**) indicated the formation of rod-like nanoparticles smaller than 100 nm in size in the presence of agglomerate clusters. The mHAp, Zn1%-mHAp, and Zn2%-mHAp samples (**Figures SM4a–SM4c**) showed pores with disordered arrangements, which occupied some domains (indicated by the yellow arrows in **Figures SM4a and SM4c**). In addition, the Zn^{2+}- samples (**Figures SM4b and SM4c**) showed mesoporous channels distributed parallel to the particles (indicated by the red dashed circles). The arrangement of these channels could be clearly observed from the HR-TEM images (indicated by the blue and purple arrows in **Figure 3**) of the Zn1%-mHAp sample. The less dense white stripes, through which the electron beam could easily pass, observed in the images represent the channels. In contrast, the darker stripes represent the walls of the HAp channels, which were dense and absorbed more electron beams during the analysis. The HR-TEM images (**Figure 3)** also show the lattice fringes of the Zn1%-mHAp sample, reflecting the periodicity of the atomic planes of the mHAp hexagonal structure [38,48], which caused the formation of tubular mesopores (as indicated by the purple arrows in **Figure 3**). Although the sample showed a disordered arrangement, its interplanar spacings could be calculated

(as indicated by the inset of **Figure 3)**, as shown in **Figure 4**. This provided a better insight into the crystal structure of the synthesized Zn-mHAp biomaterials.

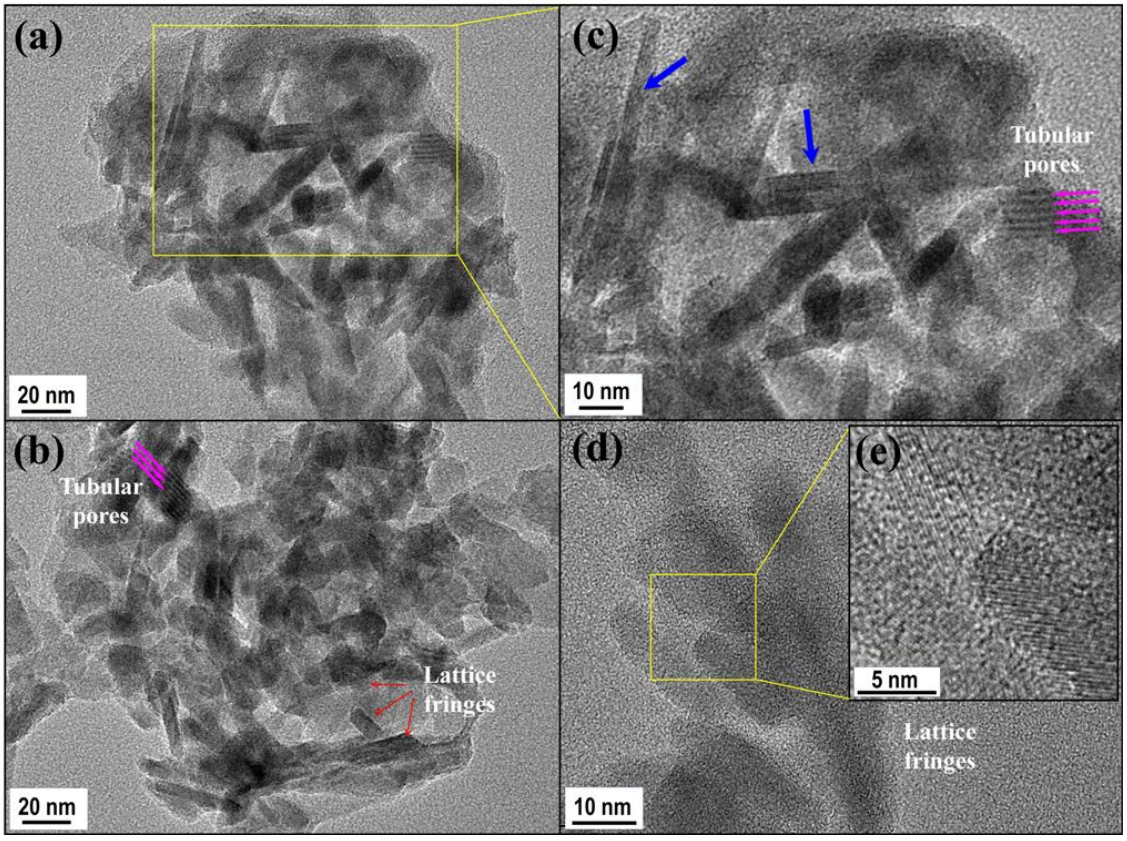

Figure 3. HR-TEM images (a, b) and high-magnification HR-TEM images (c, d) of Zn1%-mHAp showing tubular pores and lattice fringes. The inset (e) shows the clear image of the lattice fringes in this selected area.

The Zn1%-mHAp sample showed the interplanar distances (*d* spacing) of approximately 0.22, 0.27, and 0.34 nm corresponding to the (310), (300), and (002) crystallographic planes of the hexagonal HAp structure, respectively (**Figure 4)**. This

indicates that the synthesized biomaterials were polycrystalline in nature. In addition, as shown in **Figure 4**, [100] was the preferred direction for crystal growth in Zn1%-mHAp. We believe that the mHAp, Zn0.5%-mHAp, and Zn2%-mHAp samples also showed the same preferred crystal growth direction as they were synthesized using the same concentration of the casein template.

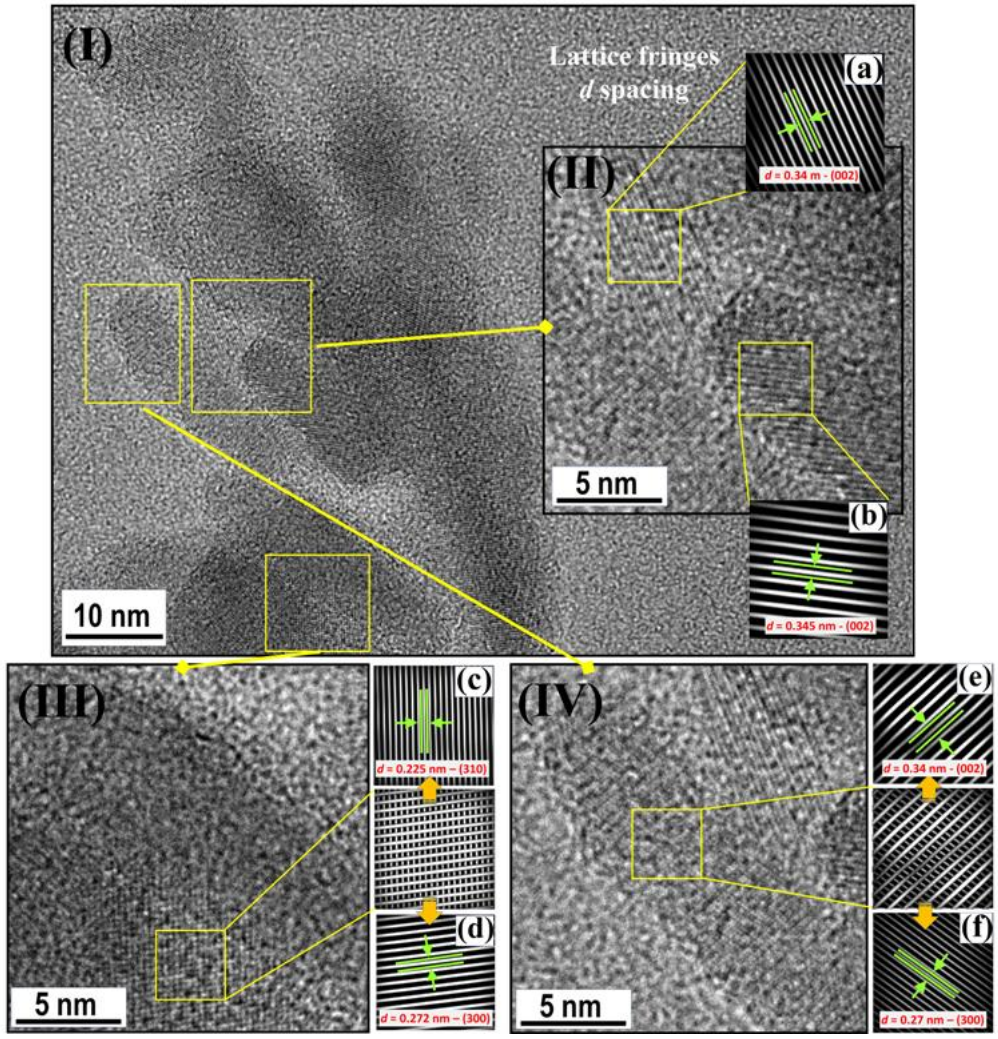

Figure 4. HR-TEM image (I) of Zn1%-mHAp and the three selected areas (I), (II), and (III) in the HR-TEM images. Images of the selected areas in the HR-TEM image after the IFFT treatment showing the crystal planes and their respective *d* spacing (a–f).

3.6 XPS analysis

The chemical nature and elemental composition of the surface of the samples were investigated by carrying out their XPS analysis, and the XPS profiles of the samples are shown in **Figure 5**. The survey and high-resolution spectra of the Zn0.5% -mHAp, Zn1% -mHAp, and Zn2% -mHAp samples were recorded.

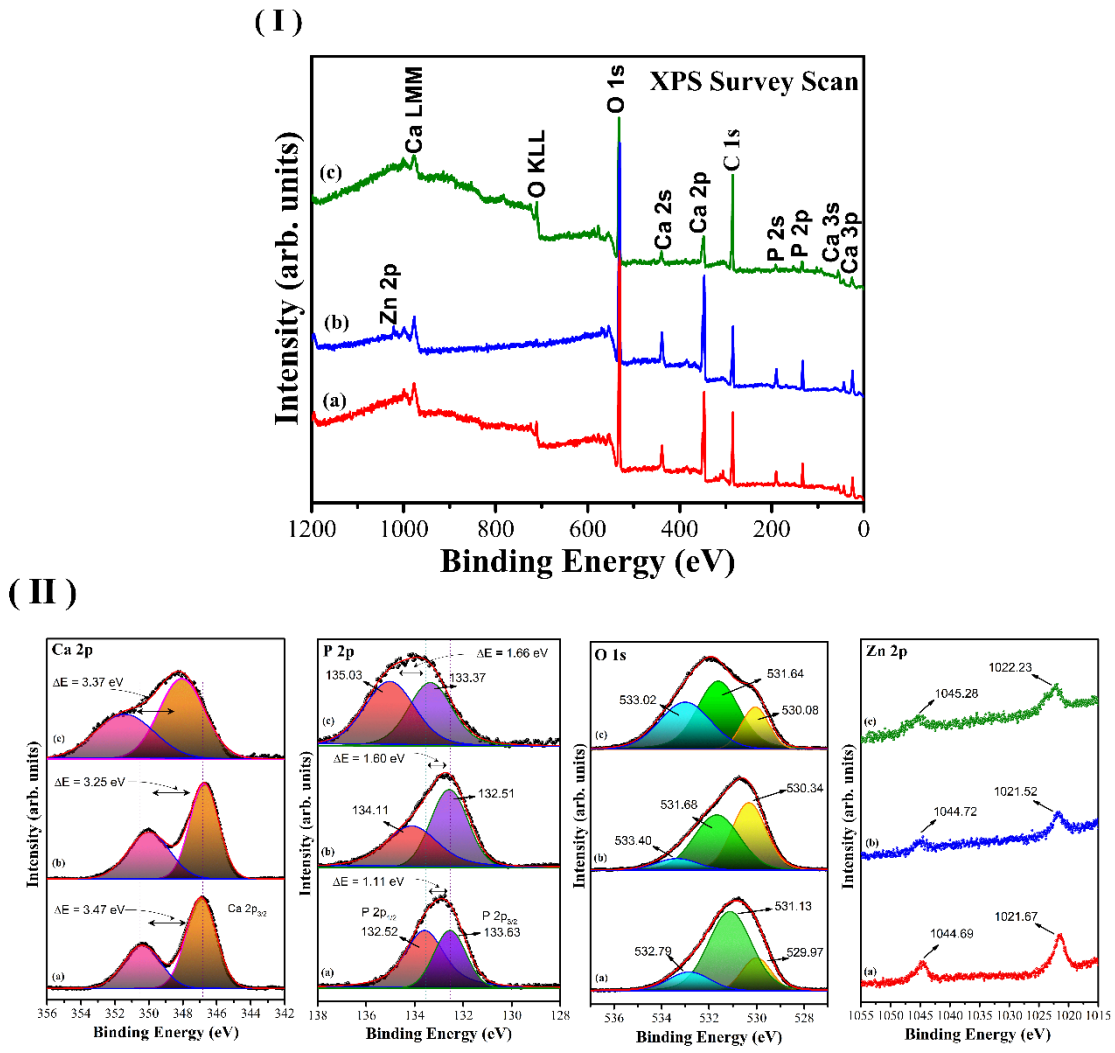

Figure 5. XPS survey profiles (I) for (a) Zn0.5%-mHAp, (b) Zn1%-mHAp, and (c) Zn2%-mHAp and high-resolution XPS scans (II) for Ca2p, P2p, O1s, and Zn2p.

The survey spectra of the samples showed the presence of Ca, P, and O corresponding to the mHAp structure. In addition, Zn was detected in the doped mHAp samples. These results confirm the successful formation of the target materials. Furthermore, all the samples showed an intense C1s signal (see also **Figure SM5**) attributed to the remaining casein anchored on the surface of the synthesized solids, as also indicated by the FTIR and TG analysis results discussed earlier. It should be noted that the emission lines of mHAp tended to shift with the incorporation of Zn, especially at higher Zn^{2+}concentrations (Zn2% -mHAp). The incorporation of Zn^{2+} into mHAp changed its local surface structural properties.

It has been reported that the high-resolution Ca2p XPS profile of HAp shows two well-defined peaks corresponding to the $Ca2p_{3/2}$ and $Ca2p_{1/2}$ orbitals [9,66,67]. These peaks were clearly observed in the present study. The high-resolution Ca2p peak of the biomaterials could be deconvoluted into two peaks, whose binding energies (BEs) varied according to the biomaterial composition. In the Ca2p spectrum of the Zn0.5%-mHAp sample, the $Ca2p_{3/2}$ and $Ca2p_{1/2}$ peaks were observed at 348.06 and 351.43 eV, respectively, and the spin-coupling energy (ΔE) was 3.37 eV. The Zn1%-mHAp (BE $Ca2p_{3/2}$ = 346.74 eV; BE $Ca2p_{1/2}$ = 349.99 eV and ΔE = 3.25 eV) and Zn2%-mHAp (BE $Ca2p_{3/2}$ = 348.06 eV; BE $Ca2p_{1/2}$ = 351.51 eV and ΔE = 3.45 eV) samples showed different BE $Ca2p_{3/2}$, BE $Ca2p_{1/2}$, and ΔE values. The Ca2p photoemission lines of the samples shifted with an increase in the Zn^{2+} content. In addition, the samples with high Zn^{2+} contents showed broad and less-defined peaks. This confirms that the Zn^{2+}/Ca^{2+}-type substitution occurred in the mHAp lattice. These results are in good agreement with those reported previously [66]. In addition, X-ray absorption near edge structure, extended X-ray absorption fine structure, and density functional theory simulation

results have demonstrated that Zn^{2+} cations preferentially occupy the Ca^{2+} sites in the HAp structure [51]. Hence, the incorporation of Zn^{2+} strongly affects the local environment of the substituted atoms, as observed in this study.

The high-resolution P2p profiles of the samples did not exhibit well-defined $P2p_{3/2}$ and $P2p_{1/2}$ components [66,67]. However, a single asymmetric peak formed by the superimposition of the two P2p components was observed. This asymmetric peak is characteristic of phosphate compounds such as HAp, and the two 2p components are associated with the phosphate groups and P-O-Ca bonds at the biomaterial surface [66–68]. Thus, the high-resolution P2p peak of the samples could be deconvoluted into $P2p_{1/2}$ and $P2p_{3/2}$ peaks. The $P2p_{1/2}$/$P2p_{3/2}$ peaks of the Zn0.5%-mHAp, Zn1%-mHAp, and Zn2%-mHAp samples were observed at 133.63/132.52, 134.11/132.51, and 135.03/133.37 eV, respectively. The variation in the BE and the broadening of the photoemission lines of the 2p components of P can be attributed to the increase in the spin-orbit coupling energy (ΔE) with Ca^{2+}/Zn^{2+} substitution. The calculated ΔE values for the Zn0.5%-mHAp, Zn1%-mHAp, and Zn2%-mHAp samples were 1.11, 1.60, and 1.66 eV, respectively. This change can be attributed to the difference in the local environment of the phosphate groups such as Zn/Ca-PO_4-OH and P-O-Ca/Zn generated upon Zn^{2+} doping.

The samples with different Zn^{2+} contents showed different high-resolution O1s profiles. The O1s peaks of the samples could be decomposed into three distinct peaks. The first peak at 531.13–531.64 eV can be attributed to the structural oxygen (O_{stru}) associated with the P (P-O) bond of HAp. The second peak at 532.79–533.40 eV corresponds to the P-O-P bonds, while the third peak observed at 529.97–530.34 eV can be attributed to the oxygen-derived species chemically adsorbed on the surface of the samples (OH^-, CO and CO_2) and the P-O-Ca/Zn interface [67,68].

As expected, the Zn2p peaks of the samples could be decomposed into two peaks corresponding to the $Zn2p_{1/2}$ and $Zn2p_{3/2}$ orbitals. The difference in the spin-orbit coupling energy (ΔE) for the Zn0.5%-mHAp, Zn1%-mHAp, and Zn2%-mHAp samples was 23.02, 23.20, and 23.05 eV, respectively, as calculated from their Zn2P XPS profiles. This indicates that Zn^{2+} was predominant in all the samples. These results confirm the successful incorporation of Zn^{2+} cations into the mHAp structure. The Zn^{2+} cations were present at the surface of the samples and the P-O-Ca/Zn interface was created.

The XPS results were consistent with the FTIR results, which indicated the presence of the P-O···Zn and P···O-Zn bonds (P-O-Zn) in the samples, especially in the Zn2%-mHAp sample. The creation of these interfaces upon Ca^{2+}/Zn^{2+} substitution changed the local coordination of Ca, P, and O at the surface of the samples, as indicated by their high-resolution XPS profiles. Therefore, the substitution of Ca^{2+} by Zn^{2+} induced an electronic disturbance at the surface of mHAp, altering its surface properties and hence functionality.

High-resolution C1s XPS profiles of the samples were also obtained (**Figure SM5**). The profiles showed three peaks at 284.0, 286.1, and 288.2 eV, attributing to the sp^2 and sp^3-hybridized carbon (C=C and C-C), hydroxyl groups (C–OH), and carboxyl (O–C =O, C=O) groups [66,67], respectively. The high intensity of the C1s peaks can be attributed to the casein remaining after the synthesis process. Moreover, the signals corresponding to the C=O and C-OH bonds can be attributed to the CO_2 and hydroxyl groups adsorbed on the surface of the samples.

3.7. Antimicrobial activity

Figure SM6 shows the images of the Petri dishes with *S. aureus* and *E. coli* bacteria after using the mHAp and Zn*x*-mHAp samples as the bacterial growth inhibitors. The results obtained by the direct contact method are shown in **Figure 6**.

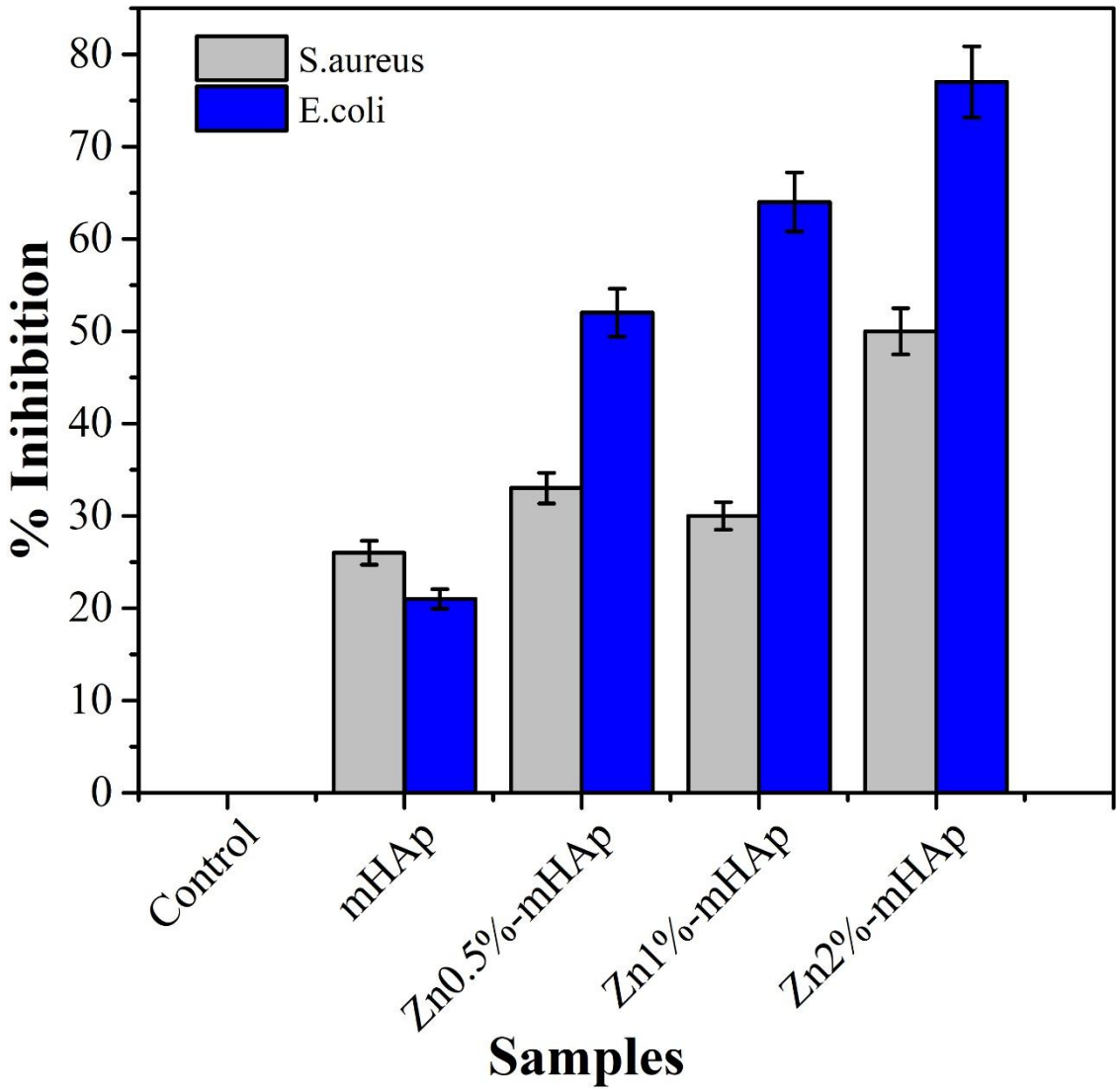

Figure 6. Bacterial growth inhibitory concentrations of the mHAp and Zn*x*-HAp samples.

The pure mHAp sample showed a growth inhibition of 26% and 21% for *S. aureus* and *E. coli*, respectively. These results can be related to the surface characteristics of the mHAp, which consisted of hydroxyl groups (a strong oxidizing agent) and the remaining casein on the surface. It is well-known that mHAp is hydrophilic and interacts with the hydrophilic groups of the bacterial cell wall, which is composed of a thick layer of peptidoglycan (a carbohydrate-conjugated amino acid copolymer) [69]. Similar behavior has been reported by Tank *et al*. [32] for *S. aureus* using pure nano-HAp. The antimicrobial activity of pure HAp against *S. aureus* and *E. coli* bacteria has also been investigated using the paper disc method [19]. The lower activity of HAp against *E. coli* can be attributed to the composition of the hydrophobic outer membrane of this bacterium. As the *E. coli* membrane is composed of amphipathic molecules such as lipopolysaccharides and phospholipids, it shows poor interaction with the hydrophilic surface of HAp. Thus, HAp shows poor growth inhibition for *E. coli* [69–71].

All the Zn^{2+}-doped mHAp samples showed higher antibacterial activity than pure mHAp, and the antibacterial efficiency of the Zn^{2+}-doped mHAp samples increased with an increase in the Zn^{2+} content. For example, the Zn2%-mHAp showed the highest antibacterial activity with a maximum bacterial inhibitory concentration of 50% for *S. aureus* and 77% for *E. coli* (**Figure 6**). In fact, the best antibacterial performance of the Zn2%-mHAp sample can be attributed to the Zn^{2+}cations present on its surface (as indicated by the XPS analysis results), which improved the surface charge properties of this material.

Various factors are responsible for the inhibition of bacterial growth by Zn*x*-HAp biomaterials. One of these factors is the particle size. The mHAp, Zn1%-mHAp, and Zn2%-mHAp samples showed the average particle sizes of 42, 27, and 26 nm (**Figure SM7**), respectively. In addition, the presence of mesoporous channels is important for the diffusion of species. These factors are fundamental and affect the antibacterial activity of Zn*x*-HAp biomaterials [72].

Despite the number of studies concerning the antibacterial activity of pure and Zn-doped HAps against gram-positive and gram-negative bacteria, different efficiency has been observed [9,32,33]. The different behavior observed among the materials might be attributed to the particle characteristics and, especially, to different surface properties, which can be strongly influenced by the type of surfactant and the amount of Zn^{2+} used to prepare the materials. In our study, lower amount of Zn^{2+}-content were incorporated to the HAp matrix in comparison to the previous reports. Moreover, Tank *et al.* [32], prepared Zn-HAps using a nonionic surfactant (Triton X-100), known to be toxic and can play a role in the bacteria inhibition growth. [73–75]. In the present work, casein phosphoprotein was used as a biotemplate to prepare Zn-mHAp biomaterials. As a result, its use as template in the synthesis of mesoporous materials for applications in biological systems cannot only enhances biocompatibility, but also can eliminate problems of toxicity of materials prepared in the presence of synthetic-type templates such as Triton X-100.

The results discussed thus far suggest that using casein (a natural phosphoprotein) as a template and Zn^{2+} as a dopant is an efficient approach to synthesize novel HAp-based biomaterials with tailored properties for specific applications.

Conclusion

Monophasic nanoparticles of pure and Zn^{2+}-doped mHAp were successfully synthesized by the co-precipitation method using casein as the template. The structural, textural, morphological, and biological characterizations of the samples confirmed the incorporation of Zn^{2+} into the HAp matrix. The use of the casein template allowed the control of the surface properties of mHAp by increasing its porosity, which improved its interaction with the bacteria through the active sites. The antimicrobial activities of the Zn^{2+}-doped mHAp against gram-positive and gram-negative bacteria were investigated. It was found that the antibacterial efficiency of the Zn^{2+}-doped mHAp depended strongly on the amount of Zn^{2+} cations incorporated into the mHAp structure and their presence on the HAp surface, as indicated by the XPS analysis results. The antimicrobial tests demonstrated the potential of the Zn^{2+}-doped HAp samples for biomedical applications, especially in the control of bacterial infections in bone repair or dental prosthesis.

Acknowledgements

The authors acknowledge CNPq/MCTIC and CAPES for financial support and CNPq for financial support in the form of research fellowships awarded to M.G. Fonseca (Grant 310921-2017-1). A. Menezes thanks CAPES for the PNPD fellowship (Grant 88882.317938/2019-01).

References

[1] Z. Breijyeh, B. Jubeh, R. Karaman, Resistance of Gram-Negative Bacteria to Current Antibacterial Agents and Approaches to Resolve It, Molecules. 25 (2020) 1340–1363. https://doi.org/10.3390/molecules25061340.

[2] A. Kubacka, M.S. Diez, D. Rojo, R. Bargiela, S. Ciordia, I. Zapico, J.P. Albar, C. Barbas, V.A.P. Martins dos Santos, M. Fernández-García, M. Ferrer, Understanding the antimicrobial mechanism of TiO_2 -based nanocomposite films

in a pathogenic bacterium, Scientific Reports. 4 (2014) 1-9. https://doi.org/10.1038/srep04134.
[3] U.L.N.H. Senarathna, S.S.N. Fernando, T.D.C.P. Gunasekara, M.M. Weerasekera, H.G.S.P. Hewageegana, N.D.H. Arachchi, H.D. Siriwardena, P.M. Jayaweera, Enhanced antibacterial activity of TiO_2 nanoparticle surface modified with Garcinia zeylanica extract, Chemistry Central Journal. 11 (2017) 1-8. https://doi.org/10.1186/s13065-017-0236-x.
[4] S. Naslapur, Sameer Ahmad Malik, L. S.M, R. C.S, The Effect of Silver Oxide Nanoparticles on the Antibacterial Property and Shear Bond Strength of Dental Composite, Dental Health: Current Research. 5 (2019) 1–10. https://doi.org/10.4172/2470-0886.1000138.
[5] Y. Xie, Y. He, P.L. Irwin, T. Jin, X. Shi, Antibacterial Activity and Mechanism of Action of Zinc Oxide Nanoparticles against Campylobacter jejuni, Applied and Environmental Microbiology. 77 (2011) 2325–2331. https://doi.org/10.1128/AEM.02149-10.
[6] A. Akbar, M.B. Sadiq, I. Ali, N. Muhammad, Z. Rehman, M.N. Khan, J. Muhammad, S.A. Khan, F.U. Rehman, A.K. Anal, Synthesis and antimicrobial activity of zinc oxide nanoparticles against foodborne pathogens Salmonella typhimurium and Staphylococcus aureus, Biocatalysis and Agricultural Biotechnology. 17 (2019) 36–42. https://doi.org/10.1016/j.bcab.2018.11.005.
[7] V. Tiwari, N. Mishra, K. Gadani, P.S. Solanki, N.A. Shah, M. Tiwari, Mechanism of Anti-bacterial Activity of Zinc Oxide Nanoparticle Against Carbapenem-Resistant Acinetobacter baumannii, Frontiers in Microbiology. 9 (2018) 1-10. https://doi.org/10.3389/fmicb.2018.01218.
[8] P. Sobierajska, A. Dorotkiewicz-Jach, K. Zawisza, J. Okal, T. Olszak, Z. Drulis-Kawa, R.J. Wiglusz, Preparation and antimicrobial activity of the porous hydroxyapatite nanoceramics, Journal of Alloys and Compounds. 748 (2018) 179–187. https://doi.org/10.1016/j.jallcom.2018.03.162.
[9] E.A. Ofudje, A.I. Adeogun, M.A. Idowu, S.O. Kareem, Synthesis and characterization of Zn-Doped hydroxyapatite: scaffold application, antibacterial and bioactivity studies, Heliyon. 5 (2019) e01716. https://doi.org/10.1016/j.heliyon.2019.e01716.
[10] A. Costescu, C.S. Ciobanu, S.L. Iconaru, R.V. Ghita, C.M. Chifiriuc, L.G. Marutescu, D. Predoi, Fabrication, Characterization, and Antimicrobial Activity, Evaluation of Low Silver Concentrations in Silver-Doped Hydroxyapatite Nanoparticles, Journal of Nanomaterials. 2013 (2013) 194854. https://doi.org/10.1155/2013/194854.
[11] M. Riaz, R. Zia, A. Ijaz, T. Hussain, M. Mohsin, A. Malik, Synthesis of monophasic Ag doped hydroxyapatite and evaluation of antibacterial activity, Materials Science and Engineering: C. 90 (2018) 308–313. https://doi.org/10.1016/j.msec.2018.04.076.
[12] J. Wang, X. Gong, J. Hai, T. Li, Synthesis of silver–hydroxyapatite composite with improved antibacterial properties, Vacuum. 152 (2018) 132–137. https://doi.org/10.1016/j.vacuum.2018.03.015.
[13] B. Priyadarshini., U. Priyadarshini., U. Vijayalakshmi., Preparation and characterization of sol-gel derived Ce^{4+} doped hydroxyapatite and its in vitro biological evaluations for orthopedic applications, Materials & Design. 119 (2017) 446–455. https://doi.org/10.1016/j.matdes.2017.01.095.
[14] P. Phatai, C.M. Futalan, S. Utara, P. Khemthong, S. Kamonwannasit, Structural characterization of cerium-doped hydroxyapatite nanoparticles synthesized by an

ultrasonic-assisted sol-gel technique, Results in Physics. 10 (2018) 956–963. https://doi.org/10.1016/j.rinp.2018.08.012.
[15] T. Nagyné-Kovács, B. Mészáros, M. Molnár, M. Tolner, I.E. Lukács, I.M. Szilágyi, G. Pokol, Hydrothermal synthesis of Sr-doped hydroxyapatite and its antibacterial activity, Periodica Polytechnica Chemical Engineering 64 (2020) 54–60. https://doi.org/10.3311/PPch.14062.
[16] M. Hadidi, A. Bigham, E. Saebnoori, S.A. Hassanzadeh-Tabrizi, S. Rahmati, Z.M. Alizadeh, V. Nasirian, M. Rafienia, Electrophoretic-deposited hydroxyapatite-copper nanocomposite as an antibacterial coating for biomedical applications, Surface and Coatings Technology. 321 (2017) 171–179. https://doi.org/10.1016/j.surfcoat.2017.04.055.
[17] T. Furuzono, M. Okazaki, Y. Azuma, M. Iwasaki, Y. Kogai, Y. Sawa, Newly Developed Biocompatible Material: Dispersible Titanium-Doped Hydroxyapatite Nanoparticles Suitable for Antibacterial Coating on Intravascular Catheters, Contributions to Nephrology 189 (2017) 144–152. https://doi.org/10.1159/000450744.
[18] G. Singh, R.P. Singh, S.S. Jolly, Customized hydroxyapatites for bone-tissue engineering and drug delivery applications: a review, Journal of Sol-Gel Science and Technology. 94 (2020) 505–530. https://doi.org/10.1007/s10971-020-05222-1.
[19] A. Anwar, S. Akbar, A. Sadiqa, M. Kazmi, Novel continuous flow synthesis, characterization and antibacterial studies of nanoscale zinc substituted hydroxyapatite bioceramics, Inorganica Chimica Acta. 453 (2016) 16–22. https://doi.org/10.1016/j.ica.2016.07.041.
[20] I. Uysal, F. Severcan, A. Tezcaner, Z. Evis, Co-doping of hydroxyapatite with zinc and fluoride improves mechanical and biological properties of hydroxyapatite, Progress in Natural Science: Materials International. 24 (2014) 340–349. https://doi.org/10.1016/j.pnsc.2014.06.004.
[21] J. Ran, P. Jiang, G. Sun, Z. Ma, J. Hu, X. Shen, H. Tong, Comparisons among Mg, Zn, Sr, and Si doped nano-hydroxyapatite/chitosan composites for load-bearing bone tissue engineering applications, Materials Chemistry Frontiers. 1 (2017) 900–910. https://doi.org/10.1039/C6QM00192K.
[22] C.L. Popa, A. Deniaud, I. Michaud-Soret, R. Guégan, M. Motelica-Heino, D. Predoi, Structural and Biological Assessment of Zinc Doped Hydroxyapatite Nanoparticles, Journal of Nanomaterials. 2016 (2016) 1-10. https://doi.org/10.1155/2016/1062878.
[23] D. Predoi, S. Iconaru, A. Deniaud, M. Chevallet, I. Michaud-Soret, N. Buton, A. Prodan, Textural, Structural and Biological Evaluation of Hydroxyapatite Doped with Zinc at Low Concentrations, Materials. 10 (2017) 229–246. https://doi.org/10.3390/ma10030229.
[24] E.S. Thian, T. Konishi, Y. Kawanobe, P.N. Lim, C. Choong, B. Ho, M. Aizawa, Zinc-substituted hydroxyapatite: a biomaterial with enhanced bioactivity and antibacterial properties, Journal of Materials Science: Materials in Medicine. 24 (2013) 437–445. https://doi.org/10.1007/s10856-012-4817-x.
[25] Y.H. Ng, Y.H. Leung, F.Z. Liu, A.M.C. Ng, M.H. Gao, C.M.N. Chan, A.B. Djurišić, F.C.C. Leung, W.K. Chan, Antibacterial activity of ZnO nanoparticles under ambient illumination — The effect of nanoparticle properties, Thin Solid Films. 542 (2013) 368–372. https://doi.org/10.1016/j.tsf.2013.05.167.
[26] V. Stanić, S. Dimitrijević, J. Antić-Stanković, M. Mitrić, B. Jokić, I.B. Plećaš, S. Raičević, Synthesis, characterization and antimicrobial activity of copper and

zinc-doped hydroxyapatite nanopowders, Applied Surface Science. 256 (2010) 6083–6089. https://doi.org/10.1016/j.apsusc.2010.03.124.
[27] F. Chen, M. Wang, J. Wang, X. Chen, X. Li, Y. Xiao, X. Zhang, Effects of hydroxyapatite surface nano/micro-structure on osteoclast formation and activity, Journal of Materials Chemistry B. 7 (2019) 7574–7587. https://doi.org/10.1039/C9TB01204D.
[28] R.A. Surmenev, M.A. Surmeneva, A.A. Ivanova, Significance of calcium phosphate coatings for the enhancement of new bone osteogenesis – A review, Acta Biomaterialia. 10 (2014) 557–579. https://doi.org/10.1016/j.actbio.2013.10.036.
[29] X. Wang, A. Ito, Y. Sogo, X. Li, A. Oyane, Zinc-containing apatite layers on external fixation rods promoting cell activity, Acta Biomaterialia. 6 (2010) 962–968. https://doi.org/10.1016/j.actbio.2009.08.038.
[30] D. Predoi, SL. Iconaru, MV. Predoi, Dextran-Coated Zinc-Doped Hydroxyapatite for Biomedical Applications, Polymers. 11 (2019) 886-902. https://doi.org/10.3390/polym11050886.
[31] P. Bhattacharjee, H. Begam, A. Chanda, S.K. Nandi, Animal trial on zinc doped hydroxyapatite: A case study, Journal of Asian Ceramic Societies. 2 (2014) 44–51. https://doi.org/10.1016/j.jascer.2014.01.005.
[32] K.P. Tank, K.S. Chudasama, V.S. Thaker, M.J. Joshi, Pure and zinc doped nano-hydroxyapatite: Synthesis, characterization, antimicrobial and hemolytic studies, Journal of Crystal Growth. 401 (2014) 474–479. https://doi.org/10.1016/j.jcrysgro.2014.01.062.
[33] I. Ullah, M.A. Siddiqui, S.K. Kolawole, H. Liu, J. Zhang, L. Ren, K. Yang, Synthesis, characterization and in vitro evaluation of zinc and strontium binary doped hydroxyapatite for biomedical application, Ceramics International. 46 (2020) 14448–14459. https://doi.org/10.1016/j.ceramint.2020.02.242.
[34] S. Atmaca, K. Gül, R. Çiçek, The Effect of Zinc On Microbial Growth, Turkish Journal of Medical Sciences. 28 (1998) 595–598.
[35] T.N. Kim, Q.L. Feng, J.O. Kim, J. Wu, H. Wang, G.C. Chen, F.Z. Cui, Antimicrobial effects of metal ions (Ag^{+}, Cu^{2+}, Zn^{2+}) in hydroxyapatite, Journal of Materials Science Materials in Medicine. 9 (1998) 129–134. https://doi.org/10.1023/A:1008811501734.
[36] B. Ahmed, B. Solanki, A. Zaidi, M.S. Khan, J. Musarrat, Bacterial toxicity of biomimetic green zinc oxide nanoantibiotic: insights into ZnONP uptake and nanocolloid–bacteria interface, Toxicology Research. 8 (2019) 246–261. https://doi.org/10.1039/C8TX00267C.
[37] L. Wang, C. Hu, L. Shao, The antimicrobial activity of nanoparticles: present situation and prospects for the future, International Journal of Nanomedicine. 12 (2017) 1227–1249. https://doi.org/10.2147/IJN.S121956.
[38] O.G. da Silva, M.M. Alves, I.M.G. dos Santos, M.G. Fonseca, M. Jaber, Mesoporous calcium phosphate using casein as a template: Application to bovine serum albumin sorption, Colloids and Surfaces B: Biointerfaces. 158 (2017) 480–487. https://doi.org/10.1016/j.colsurfb.2017.07.011.
[39] C. Qi, S. Musetti, L.H. Fu, Y.J. Zhu, L. Huang, Biomolecule-assisted green synthesis of nanostructured calcium phosphates and their biomedical applications, Chemical Society Reviews. 48 (2019) 2698–2737. https://doi.org/10.1039/C8CS00489G.

[40] P. Turon, L. del Valle, C. Alemán, J. Puiggalí, Biodegradable and Biocompatible Systems Based on Hydroxyapatite Nanoparticles, Applied Sciences. 7 (2017) 60–87. https://doi.org/10.3390/app7010060.
[41] W. Yu, T.-W. Sun, C. Qi, Z. Ding, H. Zhao, S. Zhao, Z. Shi, Y.-J. Zhu, D. Chen, Y. He, Evaluation of zinc-doped mesoporous hydroxyapatite microspheres for the construction of a novel biomimetic scaffold optimized for bone augmentation, International Journal of Nanomedicine. 12 (2017) 2293–2306. https://doi.org/10.2147/IJN.S126505.
[42] S. Brunauer, P.H. Emmett, E. Teller, Adsorption of Gases in Multimolecular Layers, Journal of the American Chemical Society. 60 (1938) 309–319. https://doi.org/10.1021/ja01269a023.
[43] E.P. Barrett, L.G. Joyner, P.P. Halenda, The Determination of Pore Volume and Area Distributions in Porous Substances. I. Computations from Nitrogen Isotherms, Journal of the American Chemical Society. 73 (1951) 373–380. https://doi.org/10.1021/ja01145a126.
[44] L.Y. Zheng, J.F. Zhu, Study on antimicrobial activity of chitosan with different molecular weights, Carbohydrate Polymers. 54 (2003) 527–530. https://doi.org/10.1016/j.carbpol.2003.07.009.
[45] M. Thommes, K. Kaneko, A.V. Neimark, J.P. Olivier, F. Rodriguez-Reinoso, J. Rouquerol, K.S.W. Sing, Physisorption of gases, with special reference to the evaluation of surface area and pore size distribution (IUPAC Technical Report), Pure and Applied Chemistry. 87 (2015) 1051–1069. https://doi.org/10.1515/pac-2014-1117.
[46] N. Abbasi Aval, J. Pirayesh Islamian, M. Hatamian, M. Arabfirouzjaei, J. Javadpour, M.R. Rashidi, Doxorubicin loaded large-pore mesoporous hydroxyapatite coated superparamagnetic Fe_3O_4 nanoparticles for cancer treatment, International Journal of Pharmaceutics. 509 (2016) 159–167. https://doi.org/10.1016/j.ijpharm.2016.05.046.
[47] H. Zhou, Y. Yang, M. Yang, W. Wang, Y. Bi, Synthesis of mesoporous hydroxyapatite via a vitamin C templating hydrothermal route, Materials Letters. 218 (2018) 52–55. https://doi.org/10.1016/j.matlet.2018.01.154.
[48] N. Pramanik, T. Imae, Fabrication and Characterization of Dendrimer-Functionalized Mesoporous Hydroxyapatite, Langmuir. 28 (2012) 14018–14027. https://doi.org/10.1021/la302066e.
[49] X. Ye, S. Cai, G. Xu, Y. Dou, H. Hu, X. Ye, Preparation and in vitro evaluation of mesoporous hydroxyapatite coated β-TCP porous scaffolds, Materials Science and Engineering: C. 33 (2013) 5001–5007. https://doi.org/10.1016/j.msec.2013.08.027.
[50] Y.J. Guo, T. Long, W. Chen, C.Q. Ning, Z.A. Zhu, Y.P. Guo, Bactericidal property and biocompatibility of gentamicin-loaded mesoporous carbonated hydroxyapatite microspheres, Materials Science and Engineering: C. 33 (2013) 3583–3591. https://doi.org/10.1016/j.msec.2013.04.021.
[51] W. Hu, J. Ma, J. Wang, S. Zhang, Fine structure study on low concentration zinc substituted hydroxyapatite nanoparticles, Materials Science and Engineering: C. 32 (2012) 2404–2410. https://doi.org/10.1016/j.msec.2012.07.014.
[52] F. Miyaji, Y. Kono, Y. Suyama, Formation and structure of zinc-substituted calcium hydroxyapatite, Materials Research Bulletin. 40 (2005) 209–220. https://doi.org/10.1016/j.materresbull.2004.10.020.

[53] F. Ren, R. Xin, X. Ge, Y. Leng, Characterization and structural analysis of zinc-substituted hydroxyapatites, Acta Biomaterialia. 5 (2009) 3141–3149. https://doi.org/10.1016/j.actbio.2009.04.014.
[54] R.M.B. Faria, D.V. César, V.M.M. Salim, Surface reactivity of zinc-modified hydroxyapatite, Catalysis Today. 133–135 (2008) 168–173. https://doi.org/10.1016/j.cattod.2007.12.114.
[55]. D Shannon, Revised Effective Ionic Radii and Systematic Studies of Interatomie Distances in Halides and Chaleogenides, Acta Crystallographica Section A. 5 (1976) 751–767. https://doi.org/10.1107/S05677394760015.
[56] O.G. da Silva, E.C. da Silva Filho, M.G. da Fonseca, L.N.H. Arakaki, C. Airoldi, Hydroxyapatite organofunctionalized with silylating agents to heavy cation removal, Journal of Colloid and Interface Science. 302 (2006) 485–491. https://doi.org/10.1016/j.jcis.2006.07.010.
[57] W. Wei, X. Zhang, J. Cui, Z. Wei, Interaction between low molecular weight organic acids and hydroxyapatite with different degrees of crystallinity, Colloids and Surfaces A: Physicochemical and Engineering Aspects. 392 (2011) 67–75. https://doi.org/10.1016/j.colsurfa.2011.09.034.
[58] T. Georgelin, M. Jaber, T. Onfroy, A.A. Hargrove, F. Costa Torro, J.F. Lambert, Inorganic Phosphate and Nucleotides on Silica Surface: Condensation, Dismutation, and Phosphorylation, The Journal of Physical Chemistry C. 117 (2013) 12579–12590. https://doi.org/10.1021/jp402437p.
[59] P.E. Timchenko, E.V. Timchenko, E.V. Pisareva, M.Y. Vlasov, N.A. Red'kin, O.O. Frolov, Spectral analysis of allogeneic hydroxyapatite powders, Journal of Physics: Conference Series. 784 (2017) 1–8. https://doi.org/10.1088/1742-6596/784/1/012060.
[60] L. Yang, W. Zhong, J. Cui, Z. Wei, W. Wei, Enhanced Removal of Cu(II) Ions from Aqueous Solution by Poorly Crystalline Hydroxyapatite Nanoparticles, Journal of Dispersion Science and Technology. 37 (2016) 956–968. https://doi.org/10.1080/01932691.2015.1077140.
[61] D.F. Mercado, G. Magnacca, M. Malandrino, A. Rubert, E. Montoneri, L. Celi, A. Bianco Prevot, M.C. Gonzalez, Paramagnetic Iron-Doped Hydroxyapatite Nanoparticles with Improved Metal Sorption Properties. A Bioorganic Substrates-Mediated Synthesis, ACS Applied Materials & Interfaces. 6 (2014) 3937–3946. https://doi.org/10.1021/am405217j.
[62] S.T. Gorgulu, M. Dogan, F. Severcan, The Characterization and Differentiation of Higher Plants by Fourier Transform Infrared Spectroscopy, Applied Spectroscopy. 61 (2007) 300–308. https://doi.org/10.1366/000370207780220903.
[63] Inamuddin, N. Shakeel, M. Imran Ahamed, S. Kanchi, H. Abbas Kashmery, Green synthesis of ZnO nanoparticles decorated on polyindole functionalized-MCNTs and used as anode material for enzymatic biofuel cell applications, Scientific Reports. 10 (2020) 5052–5062. https://doi.org/10.1038/s41598-020-61831-4.
[64] M.B.B. Pereira, D.B. França, R.C. Araújo, E.C. Silva Filho, B. Rigaud, M.G. Fonseca, M. Jaber, Amino hydroxyapatite/chitosan hybrids reticulated with glutaraldehyde at different pH values and their use for diclofenac removal, Carbohydrate Polymers. 236 (2020) 116036. https://doi.org/10.1016/j.carbpol.2020.116036.
[65] E. Adolfsson, M. Nygren, L. Hermansson, Decomposition Mechanisms in Aluminum Oxide-Apatite Systems, Journal of the American Ceramic Society. 82 (2004) 2909–2912. https://doi.org/10.1111/j.1151-2916.1999.tb02176.x.

[66] C. Negrila, M. Predoi, S. Iconaru, D. Predoi, Development of Zinc-Doped Hydroxyapatite by Sol-Gel Method for Medical Applications, Molecules. 23 (2018) 2986–3001. https://doi.org/10.3390/molecules23112986.
[67] X.-Z. Xue, J.-Y. Zhang, D. Zhou, J.-K. Liu, In-situ bonding technology and excellent anticorrosion activity of graphene oxide / hydroxyapatite nanocomposite pigment, Dyes and Pigments. 160 (2019) 109–118. https://doi.org/10.1016/j.dyepig.2018.07.057.
[68] N. Lowry, Y. Han, B.J. Meenan, A.R. Boyd, Strontium and zinc co-substituted nanophase hydroxyapatite, Ceramics International. 43 (2017) 12070–12078. https://doi.org/10.1016/j.ceramint.2017.06.062.
[69] G.T. Feitosa, M.V.B. Santos, H.M. Barreto, L.C.C. Nunes, J.A. Osajima, E.C. Silva Filho, Hydroxyapatites Obtained from Different Routes and their Antimicrobial Properties, Materials Science Forum. 869 (2016) 890–895. https://doi.org/10.4028/www.scientific.net/MSF.869.890.
[70] T.S. Araujo, S.O. Souza, E.M.B. Sousa, Effect of Zn^{2+} , Fe^{3+} and Cr^{3+} addition to hydroxyapatite for its application as an active constituent of sunscreens, Journal of Physics: Conference Series. 249 (2010) 1–7. https://doi.org/10.1088/1742-6596/249/1/012012.
[71] H. Nikaido, Molecular Basis of Bacterial Outer Membrane Permeability Revisited, Microbiology and Molecular Biology Reviews. 67 (2003) 593–656. https://doi.org/10.1128/MMBR.67.4.593-656.2003.
[72] S.M. Dizaj, F. Lotfipour, M. Barzegar Jalali, M.H. Zarrintan, K. Adibkia, Antimicrobial activity of the metals and metal oxide nanoparticles, Materials Science and Engineering: C. 44 (2014) 278–284. https://doi.org/10.1016/j.msec.2014.08.031.
[73] Â.S. Inácio, K.A. Mesquita, M. Baptista, J. Ramalho-Santos, W.L.C. Vaz, O.V. Vieira, In Vitro Surfactant Structure-Toxicity Relationships: Implications for Surfactant Use in Sexually Transmitted Infection Prophylaxis and Contraception, PLOS ONE. 6 (2011) 1–15. https://doi.org/10.1371/journal.pone.0019850.
[74] O.V. Vieira, D.O. Hartmann, C.M.P. Cardoso, D. Oberdoerfer, M. Baptista, M.A.S. Santos, L. Almeida, J. Ramalho-Santos, W.L.C. Vaz, Surfactants as Microbicides and Contraceptive Agents: A Systematic In Vitro Study, PLOS ONE. 3 (2008) 1–12. https://doi.org/10.1371/journal.pone.0002913.
[75] E. Schnitzer, M.M. Kozlov, D. Lichtenberg, The effect of cholesterol on the solubilization of phosphatidylcholine bilayers by the non-ionic surfactant Triton X-100, Chemistry and Physics of Lipids. 135 (2005) 69–82. https://doi.org/10.1016/j.chemphyslip.2005.02.002.

Figure Captions

Figure 1. (I) XRD patterns and (II) magnified XRD patterns over the 2θ range of 30–36° for (a) mHAp, (b) Zn0.5%-mHAp, (c) Zn1%-mHAp, and (d) Zn2%-mHAp.

Figure 2. Infrared spectra in the (I) 4000–400 cm^{-1} and (II) 500–1400 cm^{-1} regions for the (a) mHAp, (b) Zn0.5%-mHAp, (c) Zn1%-mHAp, and (d) Zn2%-mHap samples.

Figure 3. HR-TEM images (a, b) and high-magnification HR-TEM images (c, d) of Zn1%-mHAp showing tubular pores and lattice fringes. The inset (e) shows the clear image of the lattice fringes in this selected area.

Figure 4. HR-TEM image (I) of Zn1%-mHAp and the three selected areas (I), (II), and (III) in the HR-TEM images. Images of the selected areas in the HR-TEM image after the IFFT treatment showing the crystal planes and their respective *d* spacing (a–f).

Figure 5. XPS survey profiles (I) for (a) Zn0.5%-mHAp, (b) Zn1%-mHAp, and (c) Zn2%-mHAp and high-resolution XPS scans (II) for Ca2p, P2p, O1s, and Zn2p.

Figure 6. Bacterial growth inhibitory concentrations of the mHAp and Zn*x*-HAp samples.

Supporting information for

Zn-doped mesoporous hydroxyapatites and their antimicrobial properties

Cleibson Oliveira de Lima,[a] André L. Menezes de Oliveira,[a] Laís Chantelle,[a] Edson C. Silva Filho,[b] Maguy Jaber,[c] Maria Gardênia Fonseca[a,*]

[a]*Universidade Federal da Paraíba, Núcleo de Pesquisa e Extensão LACOM, 58051-085, João Pessoa, Paraíba, Brazil.*

[b]*Interdisciplinary Laboratory for Advanced Materials-LIMAV, Universidade Federal do Piauí, Teresina, 64049- 11 550, Piauí, Brazil.*

[c]*Sorbonne Université, Laboratoire d'Archéologie Moléculaire et Structurale, Institut Universitaire de France (IUF), CNRS UMR 8220, UPMC – Tour 23, 3ème étage, couloir 23-33, BP 225, 4 place Jussieu, 75005 Paris, France.*

Table SM1. Band assignments in the FTIR spectra of the mHAp and Zn*x*-HAp samples.

Wavenumber (cm^{-1})	Assignment
3575	ν (structural O-H)
3455	ν OH of the water
2938	asymmetric ν(C-H)
2854	symmetric ν(C-H)
1649	δ(O-H) of the adsorbed H_2O
1550	2^{nd} amide (C-N and N-H)
1456	symmetric and asymmetric ν(C-H)
1416	C-OH
1090	ν(P-O) of the PO_4^{3-}
1035	ν(P-O) of the PO_4^{3-}
960	ν(P-O) of the PO_4^{3-}
875	δ(P-O(H)) of the HPO_4^{2-}
603	δ(P-O) of the PO_4^{3-}
558	δ(P-O(H)) of the HPO_4^{2-}
522	PO_4^{3-} / Zn-O

ν – Stretching, δ – bending vibrations

Table SM2. Summary of mass losses and temperature intervals for thermal decomposition events of the synthesized samples.

Sample	Event	Mass loss (%)	Temperature (°C)
mHAp	I	2.7 ± 0.4	26-164
	II	1.8 ± 0.1	164-540
	III	1.0 ± 0.1	540-949
Zn0.5%-mHAp	I	2.5 ± 0.1	26-173
	II	1.8 ± 0.1	173-513
	III	1.5 ± 0.1	513-905
Zn1%-mHAp	I	4.1 ± 0.2	26-172
	II	1.9± 0.1	172-513
	III	1.9 ± 0.1	513-883
Zn2%-mHAp	I	3.4 ± 0.2	27-170
	II	2.1 ± 0.1	170-518
	III	1.8 ± 0.1	518-967

Figure SM1. N_2 adsorption/desorption isotherms for (a) mHAp, (b) Zn0.5%-mHAp, (c) Zn1%-mHAp, and (d) Zn2%-mHAp. The insets show the corresponding pore size distribution.

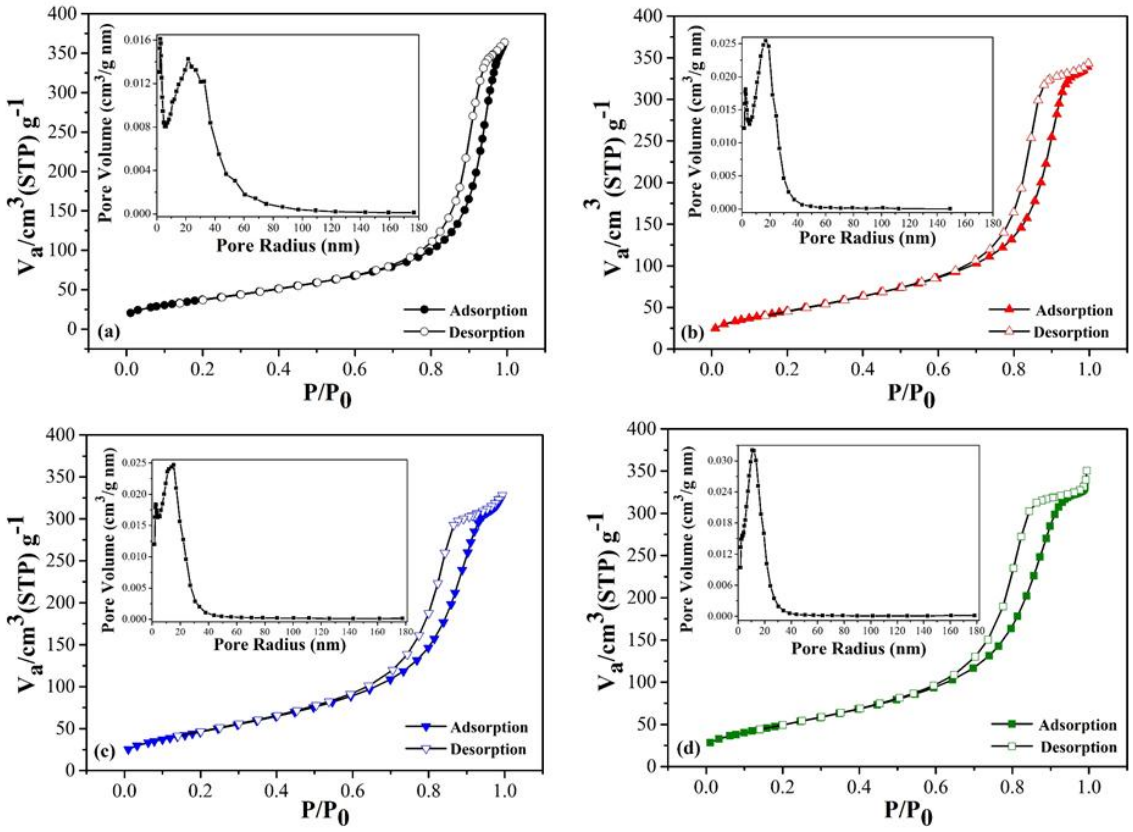

Figure SM2. Relationship between the FWHM and average crystallite size for the synthesized samples.

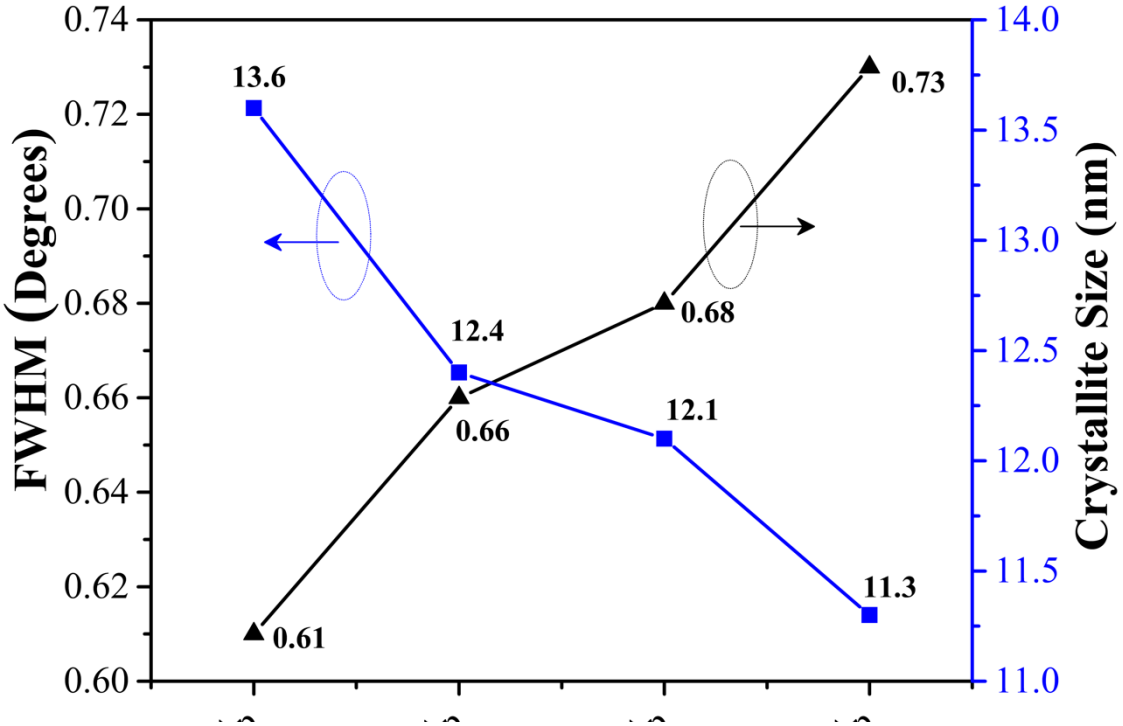

Figure SM3. TGA (DTG) curves of the (a) mHAp, (b) Zn0.5%-mHAp, (c) Zn1%-mHAp and (d) Zn2%-mHAp.

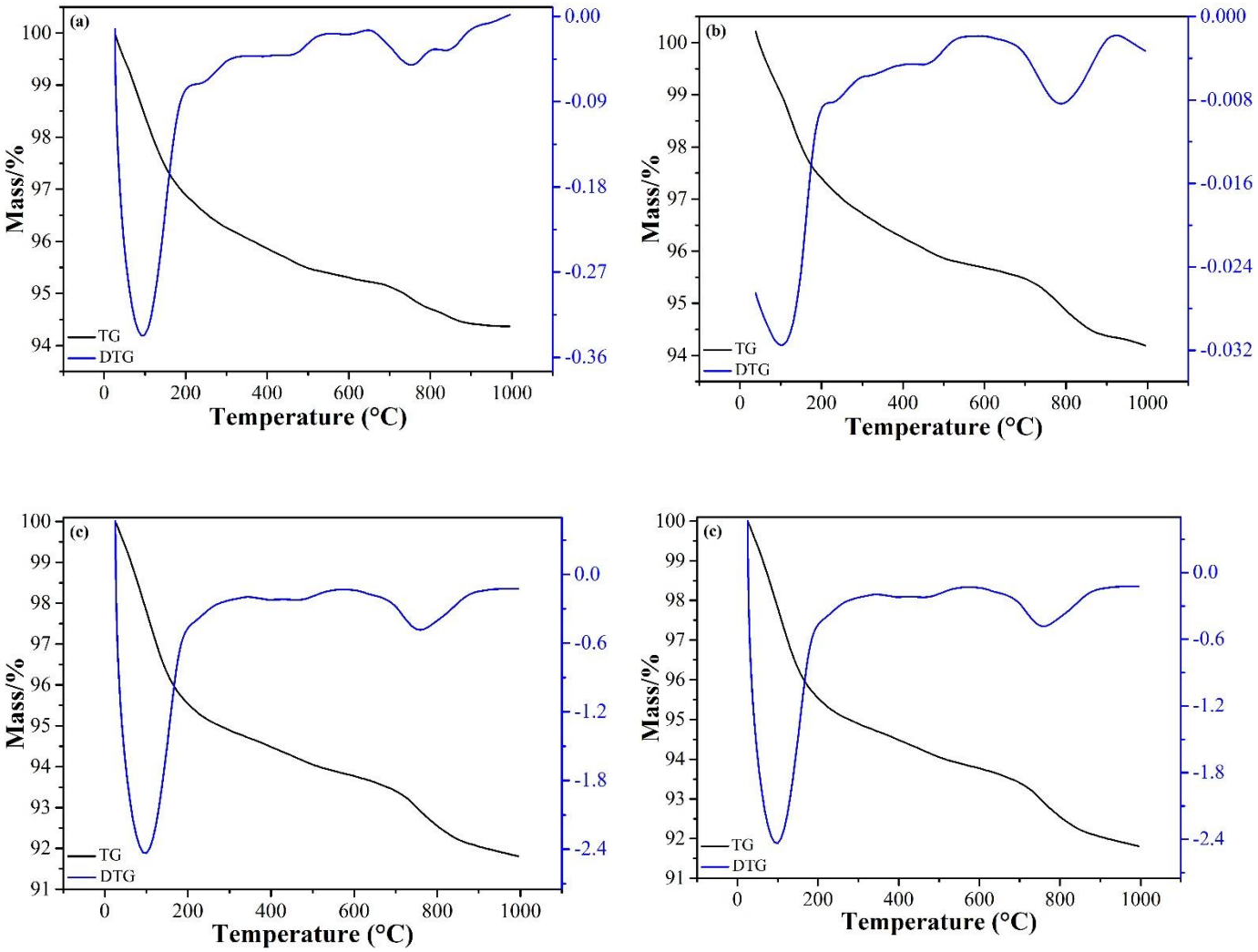

Figure SM4. TEM images of (a) mHAp, (b) Zn1%-mHAp and (c) Zn2%-mHAp.

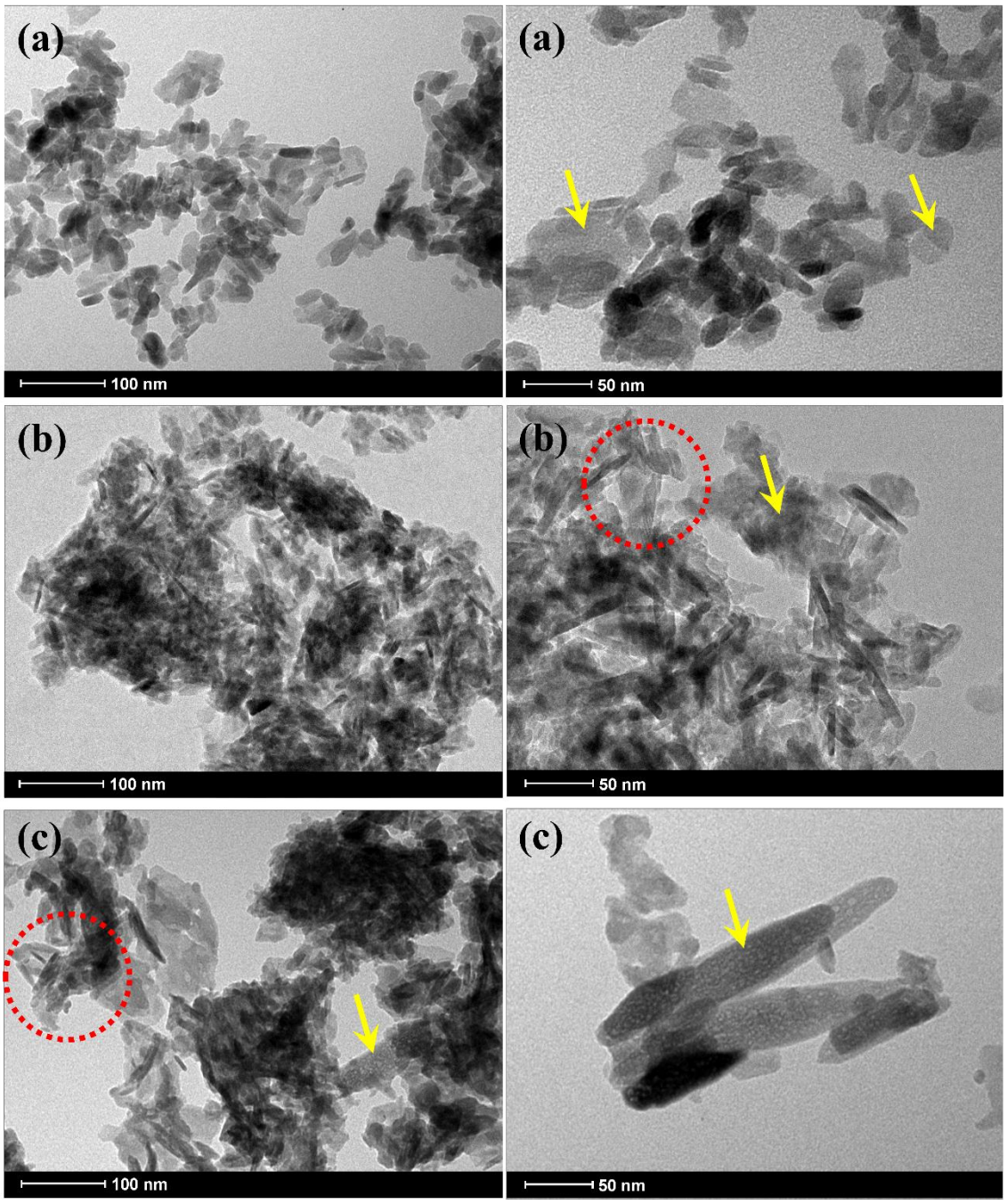

Figure SM5. High resolution XPS C1s scans for (a) Zn0.5%-mHAp, (b) Zn1%-mHAp and (c) Zn2%-mHAp.

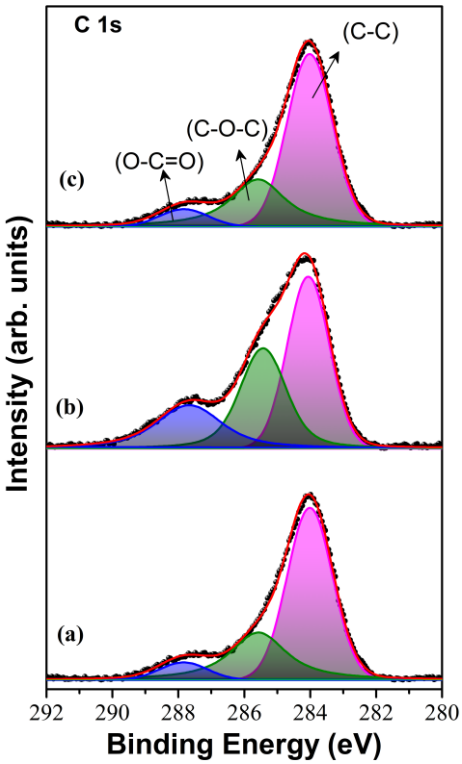

Figure SM6. Inhibitory effect of mHAp on *S. aureus* and *E. coli*.

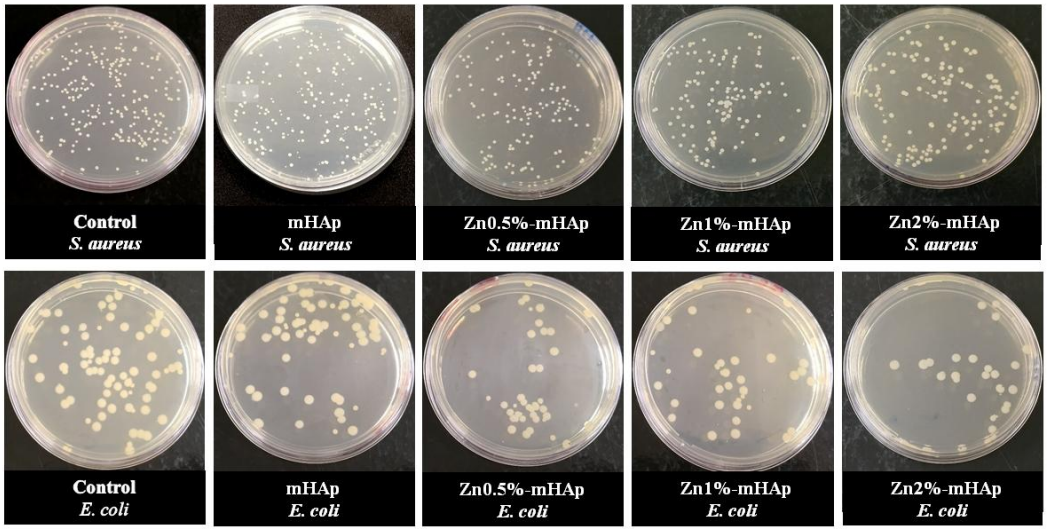

Figure SM7. Histograms of the particle size distribution for (a) mHAp, (b) Zn1%-mHAp and (c) Zn2%-mHAp.

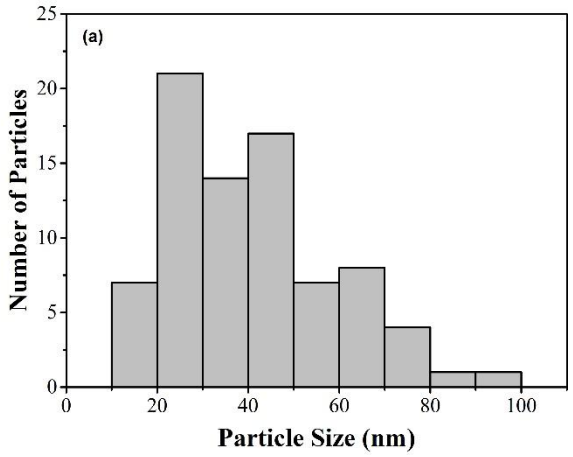

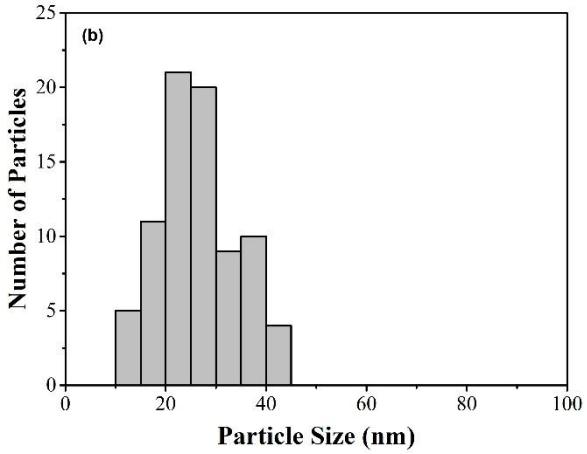

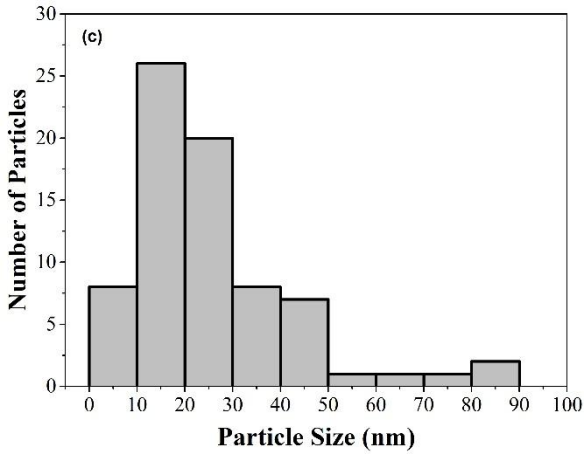

1